

UNIVERSITY COLLEGE LONDON

UPGRADE REPORT

# Lower Atmospheric Signatures of Solar Flares Associated With Sunchakes

*Jamie Ryan*

jamie.ryan.14@ucl.ac.uk

supervised by

Dr. Sarah MATTHEWS and Prof. Lucie GREEN

March 11, 2016

# Contents

<b>1</b>	<b>Introduction</b>	<b>3</b>
1.1	Solar Atmosphere . . . . .	3
1.1.1	The Photosphere . . . . .	3
1.1.2	Chromosphere . . . . .	4
1.1.3	Transition Region . . . . .	5
1.1.4	Corona . . . . .	5
1.2	Solar Magnetohydrodynamics . . . . .	5
1.2.1	Flux Tubes . . . . .	5
1.2.2	MHD Equations . . . . .	6
1.2.3	Induction Equation and the Magnetic Reynolds Number . . . . .	6
1.2.4	Plasma Beta . . . . .	6
1.2.5	Pressure Scale Height . . . . .	6
1.2.6	Magnetic Reconnection . . . . .	7
1.3	Eruptive Solar Flares . . . . .	7
1.3.1	Standard Eruptive Flare Model . . . . .	8
1.3.2	Energy Transfer . . . . .	8
1.3.3	Thick Target Model . . . . .	9
1.3.4	Hydrodynamic Response . . . . .	9
1.3.5	White Light Flares . . . . .	9
1.4	Sunquakes . . . . .	9
1.4.1	Sunquake Generation . . . . .	10
1.4.2	Local Helioseismology . . . . .	11
1.4.3	Sunquake Literature Review . . . . .	13
<b>2</b>	<b>Data and Methodology</b>	<b>15</b>
2.1	Observations and Data Reduction . . . . .	15
2.1.1	The Ramaty High Energy Solar Spectroscopic Imager . . . . .	15
2.1.2	The Interface Region Imaging Spectrograph . . . . .	15
2.1.3	The Solar Dynamics Observatorie’s Helioseismic and Magnetic Imager . . . . .	16
2.2	Data Sampling . . . . .	17
<b>3</b>	<b>Results and Discussion</b>	<b>18</b>
3.1	RHESSI Hard X-rays . . . . .	18
3.2	Emission Captured By IRIS and HMI . . . . .	19
3.3	Interpretation and Discussion . . . . .	25
3.4	Conclusions and Thesis Plan . . . . .	26
	<b>Appendices</b>	<b>27</b>
<b>A</b>	<b>Equations</b>	<b>27</b>
<b>B</b>	<b>Figures</b>	<b>28</b>

# 1 Introduction

During this age of space-born solar astronomy, understanding the highly dynamic environment of the Sun's atmosphere is a study enriched by a wealth of high detail observations. With each newly launched space instrument the spatial resolution of collected data increases, which coupled with those spacecraft that are tailored to capture light of previously unobserved wavelengths, often leads to new phenomena being observed. Eruptive solar flares fall into this category, in that spacecraft have provided observations that challenge the current theoretical view that the standard eruptive flare model (CSHKP model: (Carmichael, 1964; Sturrock, 1966; Hirayama, 1974; Kopp and Pneuman, 1976) puts forward.

Solar flares are one of the most energetic events to occur in the Sun's atmosphere, where by stored magnetic energy is released in the form of heat, mass motions, and accelerated particles. This highly dynamic process produces many measurable emission signatures at wavelengths from  $\gamma$ -rays to radio waves. Many of these observed signatures agree with the CSHKP model, however, this is not the full picture. The standard flare model has been modified to include new observations many times over the years (e.g., Shibata and Magara (2011)) and is still unable to describe some observed phenomena.

Sunquakes are an observable feature during some solar flares that the standard model is unable to explain. It is believed that they are the result of energy and momentum released during the flare impacting the lower solar atmosphere. If a sufficient amount of momentum is imparted on the lowest atmospheric layer, then acoustic waves or 'sunquakes' are produced. The challenges presented in studying this phenomena are mainly associated with the ambiguous nature of the mechanism by which sunquakes are generated. Many ideas for the sunquakes progenitors have been put forward but at this point in time observable signatures do not always show a clear cut evidence aligning with current theories. Therefore this is an exciting time to be investigating the formation mechanisms of sunquakes and could also contribute to our overall understanding of solar flares.

This work is focused on the determination of the sunquake generation mechanism for the X-class solar flare on the 29th of March 2014. The main emphasis being on whether two of the proposed sunquake progenitors (see section 1.4.1), namely direct particle beam collision and radiative backwarming, leave an energy deposition signature comparable in magnitude to the acoustic impact power at the epicentre of the seismic disturbance.

## 1.1 Solar Atmosphere

The solar atmosphere can be described as having four components, the corona, transition region, chromosphere and photosphere.

For a sunquake to occur, energy released during a solar flare has to traverse these four layers propagating through many pressure scale heights as it does so. Pressure scale height is a measure of the distance over which pressure drops off by a factor of  $e$ . For example, in the photosphere,  $H \sim 150\text{km}$ , whereas in the corona,  $H \sim 100\text{Mm}$ . Figure ?? shows how the solar atmosphere changes with height, temperature and density, for each of the atmospheric layers. Information in this section is taken from text books: Dwivedi and Parker (2003); Foukal (2004)

### 1.1.1 The Photosphere

The photosphere is the region where sunquakes manifest as observable concentric circular waves, emanating from a central impact zone. The lowest in altitude of the atmospheric layers, the photosphere forms a shell around the Sun with a radius somewhere between  $\sim 10 - 10^2 \text{ km}$ , with an effective temperature of  $T \sim 5800\text{K}$  and decreasing in temperature with radial distance to  $\sim 4400\text{K}$ , see figure ?. Emission from this part of the atmosphere is predominantly in the visible range. Contained in the photosphere, are neutral hydrogen atoms, ions and electrons. When a neutral hydrogen atom captures a free electron it forms  $\text{H}^-$  ions, which via absorption of UV and infrared radiation increases the opacity of the region. Even though it is thought that electron capture is a rare occurrence, the population of  $\text{H}^-$  ions is large enough to count for the majority of the photospheric opacity. The densest atmospheric layer, plasma pressure in the photosphere is dominant over magnetic pressure such that the plasma-beta,  $\beta = p_{\text{gas}}/p_{\text{mag}} \gg 1$ . Because of frozen-in theorem photospheric plasma dictates the motions of and to some extent, the morphology of the local magnetic field.

Granules are observed over almost the entire photosphere and are the physical representation of convection currents. Seen as the bright central part of the granule, buoyant, heated plasma rises from a region known as the convective zone, underneath the photosphere. As the material cools, it loses it's buoyancy and falls back toward the interior forming the darker areas surrounding the granule known as intergranular lanes.

Active regions on the photosphere contain sunspots, which are regions of intense magnetic field playing host to footpoints of loops that can extend out into interplanetary space. An active region is formed of at least two sunspots of opposing polarity. A sunspot is an approximately circular feature, made up of two main parts, the dark central umbra which is surrounded by the slightly lighter penumbra. The umbra hosts magnetic field lines that are tightly packed and pointing radially away from the Sun, whereas the penumbral magnetic field is more horizontal with respect to the solar surface. With a field strength of  $\sim 10^{-1}$  Tesla, sunspots are regions in the photosphere where the magnetic pressure is dominant over plasma pressure, such that  $\beta \ll 1$ . Meaning that in these regions convection currents and radiative transfer are inhibited, with the latter being the idea behind a sunspot's dark appearance.

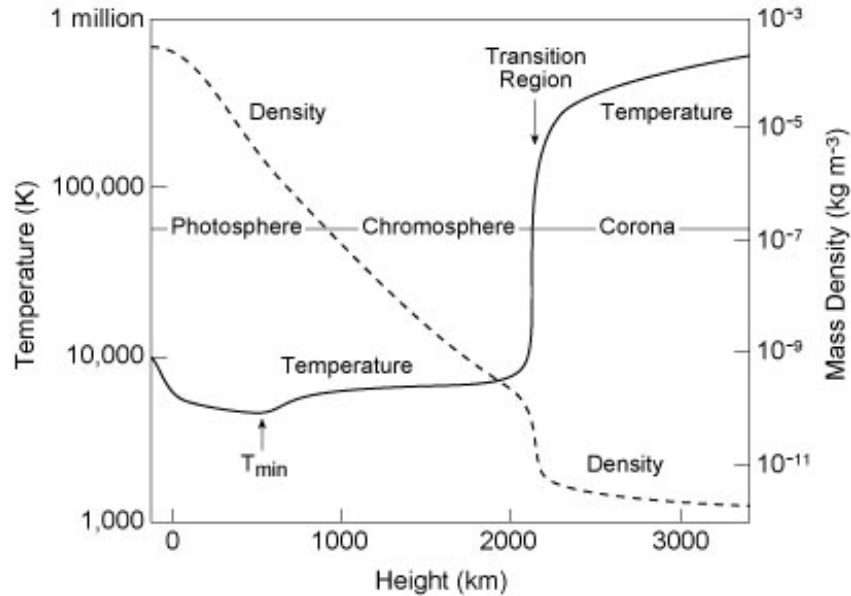


Figure 1: The temperature of the solar atmosphere decreases from values near 6,000 degrees Kelvin at the visible photosphere to a minimum value of roughly 4,400 degrees Kelvin about 500 kilometres higher up. The temperature increases with height, slowly at first, then extremely rapidly in the narrow transition region, less than 100 kilometres thick, between the chromosphere and corona, from about  $10^4$ K to about  $10^6$ K. (Courtesy of Eugene Avrett, Smithsonian Astrophysical Observatory.)

### 1.1.2 Chromosphere

The next region of the atmosphere is the chromosphere which is situated above the photosphere. Proposed sunquake generation methods (see section 1.4.1) that involve the flow of momentum through the chromosphere are shocks, radiative backwarming and direct particle collision. These progenitors would have to be able to mitigate the dissipative effects of the ever increasing plasma density throughout this region to produce a sunquake. The chromosphere is a few thousand kilometres (2000 - 3000 km) thick and is optically thin to visible light so is difficult to observe against the brightness of the photosphere. The temperature in this layer increases with height from 4400 K at the temperature minimum region to  $\sim 10^5$ K near the transition region. As a result, plasma density decreases and  $\beta$  drops, crossing unity near the transition region between the upper-chromosphere and corona. This means that the pressure scale height in this region is changing with altitude as a transition from the plasma to magnetic domain occurs. The chromosphere is observable in  $H\alpha$  line which results from photoelectric processes. Whereas collisionally produced Ca II and Mg II line emission are observable in NUV wavelengths. Sunspots still exert enough influence to control chromospheric plasma and thus are still observable. In this region, dense material suspended in magnetic fields, or filaments, can be observed in absorption, or emission at the limb (prominence). Filaments are thought to be the source of mass for coronal mass ejections (CME) due to their location over active regions and a sudden emptying of material during eruptive flares with a CME.

### 1.1.3 Transition Region

Up in altitude to the interface between the chromosphere and the corona or transition region. This region is a poorly understood layer of the solar atmosphere. What is known, is that; temperatures climb from  $\sim 10^5$  near the chromosphere to  $\sim 10^6$  K at the corona; this region has variable thickness and maybe even orientation; plasma density falls off sharply. This region can be observed in NUV wavelengths such as Si IV.

### 1.1.4 Corona

The corona is the outer most layer of the solar atmosphere, extending out into interplanetary space. This part of the atmosphere is threaded with expanded and stressed magnetic loops which are tethered at the photosphere. Stressed coronal loops store vast amounts of energy in the form of electric current, which can be released during a solar flare. At which point, energy and momentum are filtered down into deeper layers of the atmosphere, sometimes reaching all the way down to the photosphere and causing a sunquake. With a temperature ranging from  $T \sim 10^6 - 10^7$  K, this the hottest part of the atmosphere. Plasma density in this region is very low, leading to a plasma pressure which is much lower than the magnetic pressure resulting in  $\beta \ll 1$ . This means that plasma motions are dominated by magnetic fields leading to magnetic loops that can expand almost unhindered. This region is visible in UV emission by super heated plasma and via white light due to Thompson scattering of photospheric light by free electrons and dust in the coronal magnetic field.

## 1.2 Solar Magnetohydrodynamics

Most structures observed in the solar atmosphere are a direct result of interplay between plasma and the Sun's dynamic magnetic field. Understanding the relationship between a magnetic field and a plasma is important for describing the workings of solar flares, and hence could help to understand sunquakes. Magnetohydrodynamics (MHD) is a method to determine the continuous macroscopic behaviour of plasma in a magnetic field, thus individual particles are not considered (Priest, 1982). A plasma can be treated as a continuous material if distances between particles are much larger than the mean-free path, or larger than the ion gyro-radius. Where  $T$  is plasma temperature,  $\lambda_{MFP}$  is mean-free path and  $n$  is number of particles in the plasma, equation 1 describes the mean-free path.

$$\lambda_{MFP} \approx 300 \left( \frac{T}{10^6 K} \right)^2 \left( \frac{n}{10^{17} m^{-3}} \right)^{-1} m \quad (1)$$

Equation 2 is the relationship between particle mass  $m$ , velocity perpendicular to the magnetic field  $v_{\perp}$ , charge  $q$  and magnetic field strength  $B$  which governs the circular motion of a charged particle around a uniform magnetic field or the ion gyro radius.

$$r_g = \frac{mv_{\perp}}{|q|B} \quad (2)$$

In the context of the Sun, and the importance of magnetic fields for processes such as solar flares, MHD builds on the following physical assumptions; a magnetic field can manipulate a plasma by exerting a force on it. Leading to the formation of structure or movement via acceleration; a magnetic field can store the energy required for later release as a solar flare; material wrapped in a magnetic field is thermally protected from it's surroundings; a magnetic field can act as a funnel for plasma and fast particles; and finally, a magnetic field can drive instabilities and support waves (Dwivedi and Parker, 2003).

### 1.2.1 Flux Tubes

Magnetic fields are made up of discrete bundles of magnetic flux known as *flux tubes*. A magnetic flux tube can be thought of as cylindrical in geometry and containing magnetic field lines parallel in orientation to the length of the cylinder. The cross-sectional radius of the tube and magnetic field strength are both variant, magnetic flux contained within the tube however, is constant. Where  $\mathbf{B}$  is magnetic field vector and  $d\mathbf{S}$  is a cross-sectional surface element of the tube, flux  $F$  follows the relationship.

$$F = \int_S \mathbf{B} \cdot d\mathbf{S} \quad (3)$$

### 1.2.2 MHD Equations

The basics of MHD are built from a combination of Maxwell's electromagnetic equations, material equations, Ohm's law and the fluid dynamics relations. Please see section A in the appendices. Maxwell's equations and Ohm's law describe electromagnetism in terms of magnetic induction  $\mathbf{B}$ , magnetic permeability of free space  $\mu$ , electric field  $\mathbf{E}$ , electrical permittivity of free space  $\epsilon_0$ , charge density  $\rho_c$  and electric current density  $\mathbf{j}$

### 1.2.3 Induction Equation and the Magnetic Reynolds Number

The induction equation expresses the time derivative of the magnetic field in terms of its diffusion  $\eta \nabla^2 \mathbf{B}$  and advection  $\nabla \times (\mathbf{v} \times \mathbf{B})$  in the form,

$$\frac{\partial \mathbf{B}}{\partial t} = \nabla \times (\mathbf{v} \times \mathbf{B}) + \eta \nabla^2 \mathbf{B} \quad (4)$$

where magnetic diffusivity  $\eta = \frac{1}{\mu_0 \sigma}$ .

The magnetic Reynolds number,  $R_m$ , is the ratio of diffusion to advection in a magnetic field. Where  $l$ ,  $v$  and  $\sigma$  are typical length-scale, velocity and conductivity respectively,  $R_m$  can be written,

$$R_m = \frac{l_0 v_0}{\eta} \sim \frac{\nabla \times (\mathbf{v} \times \mathbf{B})}{\eta \nabla^2 \mathbf{B}} = \mu_0 \sigma v l \quad (5)$$

This ratio can be used to diagnose which part of the induction equation is dominating the MHD of the system.

If  $R_m \gg 1$  then advection is the major force changing the magnetic field, hence:

$$\frac{\partial \mathbf{B}}{\partial t} = \nabla \times (\mathbf{v} \times \mathbf{B}) \quad (6)$$

Whereas, if  $R_m \ll 1$  then diffusion is the dominant force acting on the magnetic field, leading to:

$$\frac{\partial \mathbf{B}}{\partial t} = \eta \nabla^2 \mathbf{B} \quad (7)$$

If diffusion is dominant, the magnetic field  $\mathbf{B}$  will be varying on a length-scale  $L_0$ , and so will diffuse with velocity 8, over the time-scale 9 (Dwivedi and Parker, 2003).

$$v_d = \frac{L_0}{\tau_d} = \frac{\eta}{L_0} \quad (8)$$

$$\tau_d = \frac{L_0^2}{\eta} \quad (9)$$

### 1.2.4 Plasma Beta

The plasma  $\beta$  is the ratio of plasma pressure,  $p_{plasma}$ , and magnetic pressure,  $p_{mag}$ . A measure of dominance of plasma or magnetic pressure in an MHD system can be expressed as,

$$\beta = \frac{p_{plasma}}{p_{mag}} = \frac{2p_0 \mu}{B_0^2} \quad (10)$$

so if  $\beta \ll 1$  then magnetic pressure is dominant and if  $\beta \gg 1$  then plasma pressure is dominant. In the context of the solar atmosphere, the magnetic domain of the corona has  $\beta \ll 1$  and the dense plasma domain of the photosphere has  $\beta \gg 1$ .

### 1.2.5 Pressure Scale Height

Another useful relationship to use is pressure scale height, where  $g$  is acceleration due to gravity and  $T_0$  is uniform temperature, pressure scale height,  $H = \frac{P_0}{\rho_0 g} = \frac{\Re T_0}{g}$ . When combined with pressure,  $p$  for a magneto static plasma with uniform temperature,  $p = p_0 \exp \frac{-z}{H}$ , where  $z$  is altitude, we have a measure of the height,  $H$ , over which the pressure of a plasma fall off by a factor of exp.

### 1.2.6 Magnetic Reconnection

To understand sunquakes, it is vital to comprehend the physics of eruptive solar flare events. The energy released during a flare is thought to originate from the stressed coronal magnetic field, eventually travelling to the photosphere to cause a sunquake. Magnetic reconnection (MR) is the fundamental process associated with this energy release. MR is the study of a magnetic field and it's ability to reconfigure from a high to a low energy state, as a result, it is thought to occur in many situations throughout the universe. In the context of solar physics, consider a flux tube tethered to the photosphere, which has expanded into the corona forming a loop. These extended magnetic loops can become stressed by processes such as convective motions, differential rotation, flux emergence and sun-interplanetary MR. The stressing of a magnetic field is a method of storing magnetic free energy, which can be released via reconnection which reconfigures the magnetic field to a lower (potential) energy state. Magnetic free energy released by MR, manifests in the form of accelerated particles, kinetic mass motions, heating and MHD waves, making this a highly dynamic process with many observable after effects. This is convenient in that magnetic fields cannot be observed directly, making the study of related energy release signatures important for investigating many solar MHD phenomena. For instance, the production of solar flares is thought to be driven by reconnection because many of the observed energy release signatures are explained by MR theory. Some of these signatures include emission such as  $\gamma$ -rays, hard and soft X-rays, UV, optical, microwaves and radio (See section 1.3).

**A Basic 2D model of Magnetic Reconnection.** When an electrically charged plasma exists in combination with a frozen-in magnetic field, MR is not possible because  $R_m \gg 1$  (see equation 5), meaning the diffusion term in the induction equation becomes negligible and conductivity is high. MR is only possible if electric currents are able to dissipate electric currents and thus conductivity has to drop which can happen when scale length  $l$  is decreased, if diffusivity  $\nu$  increases or if both occur. If any of these situations exists, then the time derivative of the magnetic field (induction equation 1.2) will be dominated by the diffusion term, at which point, magnetic flux will break out of the frozen-in condition and MR can occur. The location where reconnection happens is known as a magnetic null, which is a region where magnetic field strength drops to zero. This being the 2D case, the magnetic null takes on an 'X' type structure whereby two in-flowing magnetic field lines reconnect to form two out-flowing magnetic field lines. At the moment of MR, the meeting of two anti-parallel magnetic field lines causes a magnetically neutral region of continuous change from negative to positive field. This condition is sustained by the conservation of the magnetic and plasma pressure contributions from the anti-parallel field lines on either side of the continuous neutral region. Inflowing magnetic field reconnects in the diffusion region with a configuration of increased magnetic tension or curvature, which drives post-reconnection outflow of the newly connected field.

### 1.3 Eruptive Solar Flares

Solar flares are the explosive conversion of magnetic energy into mass motions, radiation, electric currents and MHD waves. These events are the most energetic of solar phenomena and can be observed throughout the entire solar atmosphere, with some of the larger flares releasing up to  $10^{37}$  erg of energy. Flares are classified by the the Geostationary Operational Environmental Satellite (GOES) see Table 1, in this stem, the logarithmic measure of 1 to 8 Å X-ray flux produced by the flare determines it's classification. The GOES system classes flares from X to A-class, in order of high to low flux, so an X-class flare event would be more powerful than an M-class and so on.

Classification	Peak Flux Range at 1 to 8 Å ( $W.m^{-2}$ )
X	$10^{-3} - 10^{-4}$
M	$10^{-4} - 10^{-5}$
C	$10^{-5} - 10^{-6}$
B3	$10^{-6} - 10^{-7}$
A	$< 10^{-7}$

Table 1: shows the GOES flare classification, which is based on the order of magnitude of hard x-ray flux. X class flares produce a flux of  $10^{-3} - 10^{-4} W.m^{-2}$  and are the most powerful, whilst a weak A class flare can produce less than  $10^{-7} W.m^{-2}$ .

### 1.3.1 Standard Eruptive Flare Model

The standard solar flare theory, also known as the CSHKP model, is the culmination of research by many authors, (Carmichael, 1964; Sturrock, 1966; Hirayama, 1974; Kopp and Pneuman, 1976), describing the formation and evolution of two-ribbon flares.

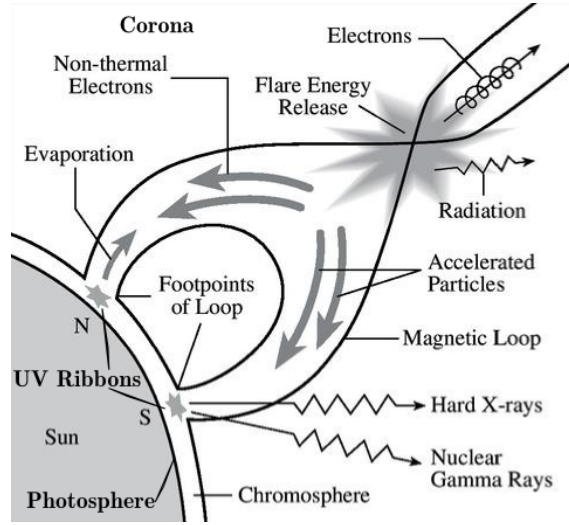


Figure 2: cartoon of the standard 2D solar flare model. Image courtesy of [www.tufts.edu](http://www.tufts.edu)

In this model, magnetic free energy is stored high up in the corona, built up by a filament rising through the atmosphere. A filament is cool dense plasma suspended in the corona overlying an active region's polarity inversion line (Babcock and Babcock, 1955). It is thought that filaments are suspended up in the corona by magnetic fields in the form of either a sheared arcade or a flux rope which is the focus of the CSHKP model. As the filament (flux rope) rises, it drags the surrounding magnetic loops along with it, which creates a situation where the legs of the loops start to flow inward. As this inward flow causes opposing magnetic legs to get closer to each other, a current sheet develops which stretches along the neutral region. This current sheet eventually becomes thin enough that magnetic reconnection occurs, reconfiguring the magnetic field from inflowing legs to outflowing flare loop and filament structure. At this point energy is released in the form of heating, accelerated particles and MHD waves. Heating can reach temperatures of  $10^7$  K and accelerated particles travel down flare loops causing emission, shocks and sometimes acoustic disturbances in the solar interior or sunquakes. The appearance of two flare ribbons is caused by reconnection occurring simultaneously across an arcade of magnetic loops. Accelerated particles travel down each loop in the arcade, colliding with the chromosphere as they do, at which point bremsstrahlung and  $H\alpha$  emission are produced, leading to the appearance of footpoints and ribbons respectively. A cascade of these reconnection events occur as the erupting filament rises through each successive loop making up the overlying non-potential magnetic field. When applied to the entire arcade of loops making up the field this leads to the appearance of flare ribbons moving outward from the polarity inversion line. If a filament is not present, Aschwanden (2005) describes the build up of magnetic free energy as being caused by the evolution of the associated active region, whereby photospheric plasma motions shear the magnetic field arcade causing reconnection.

### 1.3.2 Energy Transfer

The impulsive phase of a solar flare occurs when energy near the reconnection X-point is transported along the magnetic field into the chromosphere. The two basic methods of energy transport during this phase are thermal and non-thermal. In the thermal case, plasma in the top of a flare loop is heated by MR or shocks. In the non-thermal case, particles are imparted enough energy to no longer be described by the thermal Maxwellian distribution, instead exhibiting nonthermal energies. The energy source for nonthermal particles is thought to be MR. During the impulsive phase of a flare, electrons are accelerated to high energies, down newly reconfigured flare loops. These high energy electrons are fed into the dense plasma of the chromosphere and photosphere where they deposit their energy. The collisional thick target model by Brown (1971) says that almost all of the flare energy is carried by the particle beam, therefore, energy dissipated in the lower atmosphere represents a large portion of the flare energy budget.



### 1.3.3 Thick Target Model

Assuming that the chromosphere is a thick target, the deposition of energy by accelerated particles is due to collisions between charged particles and ions producing hard X-ray bremsstrahlung emission (Korchak, 1967). Using the thick target model (Brown, 1971) one can calculate the power,  $P_e$ , injected into the atmosphere by non-thermal electrons.

$$P_e(E \geq E_c) = \int_{E_c}^{\infty} EF(E)dE \quad (11)$$

The electron distribution  $F(E)$  is controlled by the power law  $AE^{-\delta}$ , where  $E$  is the electron energy,  $A$  is the total injected electron rate normalisation factor,  $E_c$  is the low energy cut off and  $\delta$  is the electron distribution spectral index. The value of  $E_c$  represents the upper boundary between thermal and non-thermal energy contributions to the x-ray spectrum. This means that the total energy associated with non-thermal electron power is a lower limit. Performing the integral in equation 11 gives the total non-thermal electron power in the form of equation 12.

$$P(E \geq E_c) = \frac{AE_c^{(2-\delta)}}{(\delta - 2)} \quad (12)$$

### 1.3.4 Hydrodynamic Response

During the impulsive phase of a solar flare, high energy nonthermal electrons are accelerated into the chromosphere. These particles transfer energy to the ambient chromospheric plasma in the form of heat. A consequence of this is the production of a hydrodynamic response in the form of coronal upflows and chromospheric downflows. The upflow is hot chromospheric plasma responding to an increase in temperature by expanding up into the flare loop coined as *chromospheric evaporation*. Coronal upflows emit in soft x-rays. The downflow or *chromospheric condensation* is formed when a steep temperature jump propagating into the chromosphere forms a downward moving shock front. The shock front contains dense, cool plasma which emits  $H\alpha$  (Livshits et al., 1981; Canfield et al., 1990; Kowalski et al., 2015).

### 1.3.5 White Light Flares

In 1859 the first white light flare (WLF) was observed by Carrington (1859). WLFs occur when energy is transported deep into the dense lower atmosphere causing a continuum enhancement in wavelengths with  $\lambda > 3600$  (Neidig and Cliver, 1983). Once thought as rare, work by Matthews et al. (2003) helped to show that WLFs are not only associated with the most energetic of solar flares but many of the smaller events as well. Since that first glimpse, the frequency of observations of WLFs have become common mainly due to ever increasing resolution of solar data.

Theories that have been put forward to explain WLFs credit Balmer and Paschen continuum emission from free-bound transitions in hydrogen or  $H^-$  processes (Svestka, 1976). In fact the emission process producing the white light enhancement dictates where in the atmosphere the emission is coming from. If the WLF is due to hydrogen free-bound emission, this is caused by a temperature increase of  $\sim 10^4$  K in a plasma with a hydrogen number density of  $n_H > 10^{14} \text{ cm}^{-3}$  meaning WL must be coming from deep in the chromosphere. These conditions produce the opacity required to outshine the background photosphere emission. Whereas, if the WLF is due to  $H^-$  processes the emission is coming from the photosphere where a modest temperature increase of  $\sim 10^2$  K and a hydrogen number density of  $n_H > 10^{16} \text{ cm}^{-3}$  are sufficient to satisfy opacity requirements. It is also possible that both WLF flare processes can occur simultaneously, so called radiative backwarming. Balmer/Paschen continua photons emitted in the chromosphere irradiate the photosphere and are absorbed by  $H^-$  ions which release emission causing the  $10^2$  K temperature increase in the upper photosphere (Machado et al., 1989). It is also thought that it is possible to produce WLFs by heating of the upper photosphere by energetic electron beam (Hudson, 1972) and proton beam (Machado et al., 1978).

## 1.4 Sunquakes

A sunquake occurs when acoustic waves propagate into sub-surface layers of the Sun (see Figure 3a). As acoustic wave-fronts travel into the interior they encounter layers of increasing density causing refraction back toward the solar surface (see Figure 3b). At which point, waves can be observed as circular formations in the surface

plasma, expanding outward from a point of origin (see Figure 4) (Kosovichev, 2014). Expansion of sunquake ripples accelerates as the source of leading edge of the circular wave is coming from increasingly deep layers inside the Sun. This effect is caused by the increase in density with internal depth, which leads to a rise in sound speed (Kosovichev and Zharkova, 1998). It is not unreasonable to suspect that all solar flares produce some level of seismic signature but due to sunquake waves being hard to spot against photospheric background noise, only those with sufficient amplitude are detected. Sunquake morphology can sometimes be anisotropic in that some regions in a wavefront may have a variety of amplitudes, an attribute that is credited to sub-surface deviations in refraction. The anisotropy also extends to the formation of sunquake wavefronts that are not perfectly circular which is thought to happen as a result of moving impact sites (Kosovichev, 2006).

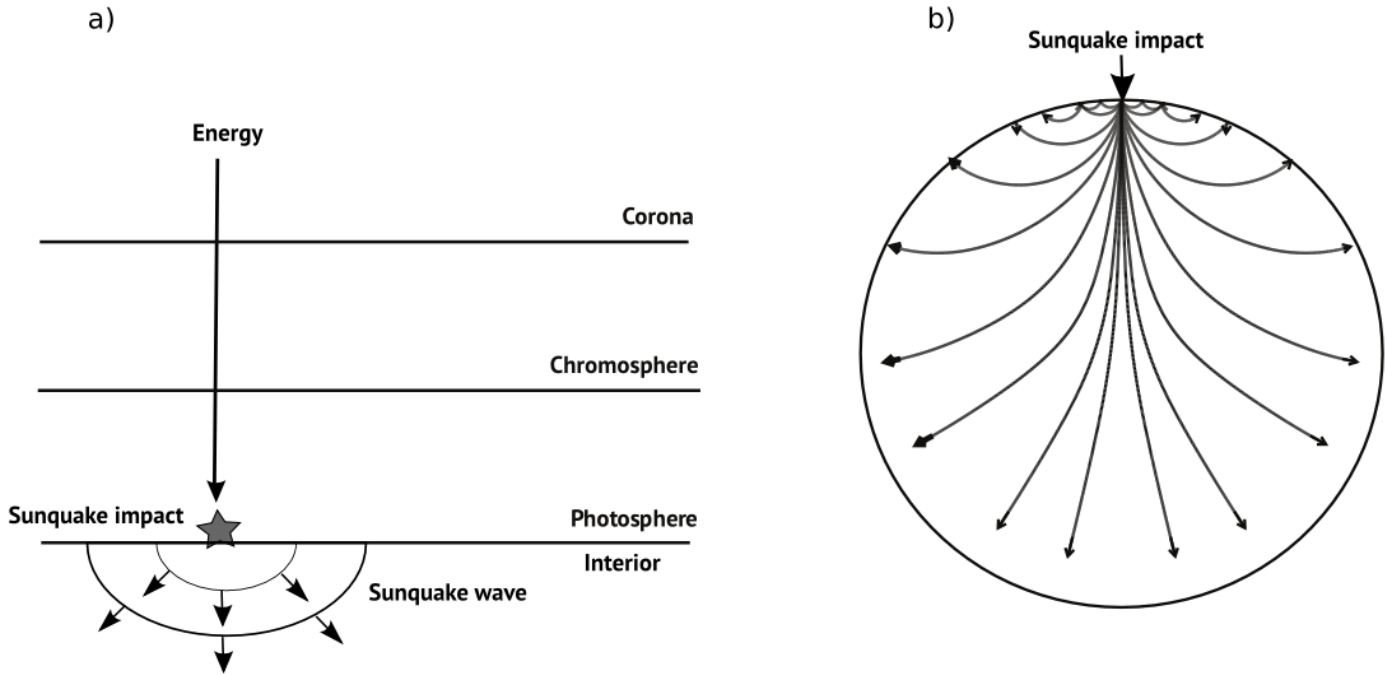


Figure 3: Sunquake cartoon: a) Shows how energy and momentum must traverse through the solar atmosphere before impacting the photosphere to generate a sunquake. b) Shows acoustic wave-fronts propagating into the interior of the Sun. Wave-fronts refract back toward the surface as they encounter increasingly dense sub-surface layers. Waves reaching the surface disturb material in a pattern resembling ripples in a pond. Courtesy of Kosovichev (2014)

#### 1.4.1 Sunquake Generation

The progenitors of sunquakes are still unknown and as a result this is an exciting area of research with discoveries still to be made. The general consensus, in terms of valid mechanisms that could cause this phenomenon is an area of contention, however the following progenitors are thought to be at least partly responsible. Each mechanism is associated with different observable signatures of which each observed sunquake may have some, none or many. This means that a rigid description of the transport of flare energy and momentum to the sub-photosphere is probably unlikely. Instead each candidate progenitor may play a bit part in the process, and there very well maybe mechanisms yet undiscovered.

- **Radiative backwarming** as a mechanism for producing sunquakes, was first put forward by Donea and Lindsey (2005) to account for a spatial correlation between seismic sources and white light emission from the lower atmosphere. During a solar flare, high energy electrons and photons impulsively heat the chromosphere and photosphere leading to an enhancement in white light emission (Machado et al., 1989). This WL enhancement can be generated by either; Balmer continuum generated by hydrogen bound-free emission in the upper-chromosphere, which irradiates the photosphere increasing local plasma temperature;  $H^-$  emission at deeper altitudes, near the temperature minimum region. In both cases, an impulsive

increase in radiation pressure and gas pressure exerted on the photosphere could generate acoustic waves which propagate into the sub-photosphere. Therefore a clear radiative energy contribution from Balmer continuum and general white light emission are considered signatures of radiative backwarming. For backwarming to be responsible for the sunquake, a comparable radiative energy budget in a Balmer or white-light signature would be required.

- **Sudden magnetic field reconfiguration** was first detailed by Hudson et al. (2008). Solar flares are violent physical processes dictated by the interplay between reconnecting magnetic fields and charged solar plasma. If the magnetic field close to the photosphere relaxes to a more horizontal alignment it can impart a Lorentz force on the local plasma environment, resulting in the production of acoustic waves in the sub-photosphere. The key parameter for this mechanism seems to be that the field has to reconfigure in an sufficiently impulsive manner to generate enough force to induce seismic waves. An observable signature of this progenitor would be impulsive changes in magnetic field strength close to the sunquake.
- **Shocks** are a mechanism originally proposed in initial work by Kosovichev and Zharkova (1995) and Kosovichev and Zharkova (1998), whereby a shock wave propagates from the upper-chromosphere down to lower altitudes. During a solar flare, particles and heat are directed down toward the chromosphere, at which point chromospheric material reacts by increasing in temperature. This increased temperature causes explosive ablation of chromospheric material both upward and downward. The downward component develops into a shock front carrying energy to the lower atmosphere, which can go on to impact the photosphere generating acoustic waves. If the shock is dissipated at higher altitudes such as the lower chromosphere, heat generated during the deposition process can irradiate the photosphere with high energy photons, causing radiative backwarming (Machado et al., 1989). If the sunquake is caused by a shock then acoustic impacts should occur approximately 100 seconds after the HXR signature associated with the flare impulsive phase, as dictated by the thick target model. Observational signatures of shocks are red or blue shifted wavelengths which can be captured in Dopplergrams or spectroscopic data.
- **Direct particle collision**, is linked to early work by Kosovichev and Zharkova (1998) and observations by Zharkova and Zharkov (2007) where the sunquake was spatially aligned with HXR and  $\gamma$ -ray emission respectively. HXRs are due to the presence of a nonthermal accelerated electron beam giving up collisional energy to the chromosphere. Whereas  $\gamma$ -rays during a solar flare are an indicator of energetic protons being accelerated along a newly reconfigured magnetic field. Proton beams carry more momentum than electron beams and are able to penetrate through the solar atmosphere to lower altitudes, therefore being more likely to cause a sunquake. If a nonthermal beam of electrons or protons makes it down to the photosphere, it can deposit energy in the form of an acoustic impact which propagates into the subphotosphere. HXRs and  $\gamma$ -rays are both observable by the Ramaty High Energy Solar Spectroscopic Imager (RHESSI), see section 2.1.1.

#### 1.4.2 Local Helioseismology

Helioseismology is a tool for probing the interior of the Sun. Most techniques in this field of analysis rely on observations of gravity and acoustic waves on the photosphere that are the result of interior excitation. Studying the frequency and modes of these oscillations has revealed much about the internal structure of the Sun. Local helioseismology is a collection of techniques developed for global helioseismology that have been modified for use in studying local regions in higher spatial resolution. The following section provides an introduction to some of these techniques.

**Theoretical Helioseismic Response** The localised helioseismic response to an impact that generates a sunquake can be calculated. If the surface impact occurs in a small volume, the radial component of the resulting helioseismic velocity,  $v_r$  can be calculated with:

$$v_r(R, \theta, \phi, t) = \sum_{nlm} \frac{P_0}{M_\odot I_{nl}} (2l+1) P_l(\cos \theta) \cos(\omega_{nl} t) e^{-\gamma_{nl} t} \quad (13)$$

The total momentum transferred by the impact is  $P_0$ ,  $M_\odot$  is solar mass,  $I_{nl}$  is the mode inertia,  $P_l$  is the Legendre polynomial,  $\omega_{nl}$  are the mode eigenfrequencies,  $\gamma_{nl}$  are their damping times and  $(2l+1)$  is a geometric factor. The collective terms  $M_\odot I_{nl}$  are known as the *mode mass* meaning that the mode amplitude driven by the impact is proportional to the total momentum over the mode mass.

$$v_r(R, \theta, \phi, t) \propto \sum_{nlm} \frac{P_0}{M_\odot I_{nl}} \quad (14)$$

A total momentum of  $10^{24}$  g.cm/s was calculated by Kosovichev (2009) as the momentum associated with the maximum observed amplitude in a sunquake. Using this technique, it is possible to extract the frequency at which wave amplitude is at a maximum, which turns out to be in the 4 to 5 mHz range.

**Helioseismic Holography** Donea et al. (1999) pioneered the use of helioseismic holography to produce seismic images of the solar flare of July 1996 reported to have a sunquake by Kosovichev and Zharkova. Time series egression-power maps at 3.5 and 6 mHz were computed with a 2 mHz bandwidth. It was found that the most powerful acoustic power frequency associated with the flare is centred at 3.5 mHz but has a large amount of noise. However, the 6 mHz range has a much lower ambient noise, therefore producing a better rendering of the seismicity of the flare. It is now standard practice to use the 6 mHz range for helioseismic holographic calculations of egression-power.

Originally the idea of analysing Doppler images of the solar surface in order to observe acoustic sources was put forward by Roddier (1975). Helioseismic holography was developed further in concept by Lindsey and Braun (Lindsey and Braun, 1990; Braun et al., 1992; Lindsey and Braun, 1997) in an effort to to image the solar interior and far-side of the Sun. This technique involves using a Doppler image of a location on the solar surface as a reference wave-field to enable an estimation of that wave-field at a location in the solar interior at a time preceding or proceeding the image. This is achieved by calculating the ingression or egression of the wave-field by assuming that it's evolution is a, convergence to, or divergence from, the point of origin of that wave-field. The technique uses Green's function (eqn 15, where  $\mathbf{r}$  and  $t$  are position and time of an observed signal and  $\mathbf{r}'$  and  $t'$  are the position and time of the signal earlier in time) which assumes that the acoustic wave propagates from a point source, allowing a signal  $\psi(\mathbf{r}, t)$  observed on the surface to be devolved backwards in time.

$$G_+(|\mathbf{r} - \mathbf{r}'|, t - t') \quad (15)$$

Where  $a$  and  $b$  constrain the holographic pupil, equation 16 is then used to devolve the surface signal to calculate the position of subsurface acoustic sources.

$$H_+(\mathbf{r}, z, t) = \int dt' \int_{a < |\mathbf{r} - \mathbf{r}'| < b} d^2\mathbf{r}' G_+(|\mathbf{r} - \mathbf{r}'|, t - t') \psi(\mathbf{r}', t') \quad (16)$$

Equation 17 is then used to calculate the egression power associated with the acoustic sources at a time  $t$ .

$$P(z, \mathbf{r}) = \int dt |H_+(\mathbf{r}, z, t)|^2 dt \quad (17)$$

If egression power is required in terms of frequency then equation 17 can be Fourier transformed into frequency space.

**Time-Distance** The first observation of a sunquake (Kosovichev and Zharkova, 1998) used the time-distance technique to track sunquake wavefronts. The paper by Duvall et al. (1993) explains how to extract time-distance (TD) information from observations of intensity fluctuations on the solar surface. This technique uses travel times of waves between two locations on the solar surface. The method assumes that the travel time of a wave propagating in the interior of the Sun will be modified by any anomalies that it has to travel through, thus the resulting signal will contain the signatures of those irregularities. For instance, if the wave encounters a flow along it's path of travel, it will propagate faster with the flow than against it, affecting travel time. This technique remaps Dopplergrams into polar coordinates, with the point of origin centred on the area of downflowing material during the flare. This remapped image is then Fourier transformed with respect to azimuthal angle, with the resulting image highlighting circular disturbances as a line of positive slope.

### 1.4.3 Sunquake Literature Review

The idea that solar flares can cause acoustic waves inside the Sun was originally put forward by (Wolff, 1972). Wolff made the connection that a large solar flare releasing enough energy to heat the photosphere, would generate expansion of photospheric material, which could lead to an impulsive stimulation of oscillations in the Sun's interior. Wolff also commented that it would be difficult to observe interior oscillations with current (in the 1970s) solar velocity measurement techniques.

A little over twenty years later and Wolff's idea was built upon by Kosovichev and Zharkova (1995), who showed theoretically that acoustic waves in the solar interior could be generated by a large solar flare, and that they may be detectable. A year later and the first detection of a sunquake was made by Kosovichev and Zharkova (1998) during an X class solar flare on July the 9th 1996. Their observational data came from the Solar and Heliospheric Observatory (SOHO) via the Michelson Doppler Imager (MDI) which images the movement of photospheric material by analysing shifts in wavelength of the emitted light. They observed a prominent impulsive downward signature in the Dopplergrams directly over a compact point source which subsequently emanates a set of concentric acoustic waves (see Figure 4). The timing of maximum downward velocity of material derived from the Dopplergrams was out of sync with peak hard x-ray measurements by around a minute. This time delay, coupled with white-light enhancement in the lower atmosphere led to the conclusion that during the flare, accelerated energetic particles heat the cool dense chromosphere causing a shock front which travels downward, depositing energy in lower atmospheric layers, generating a sunquake.

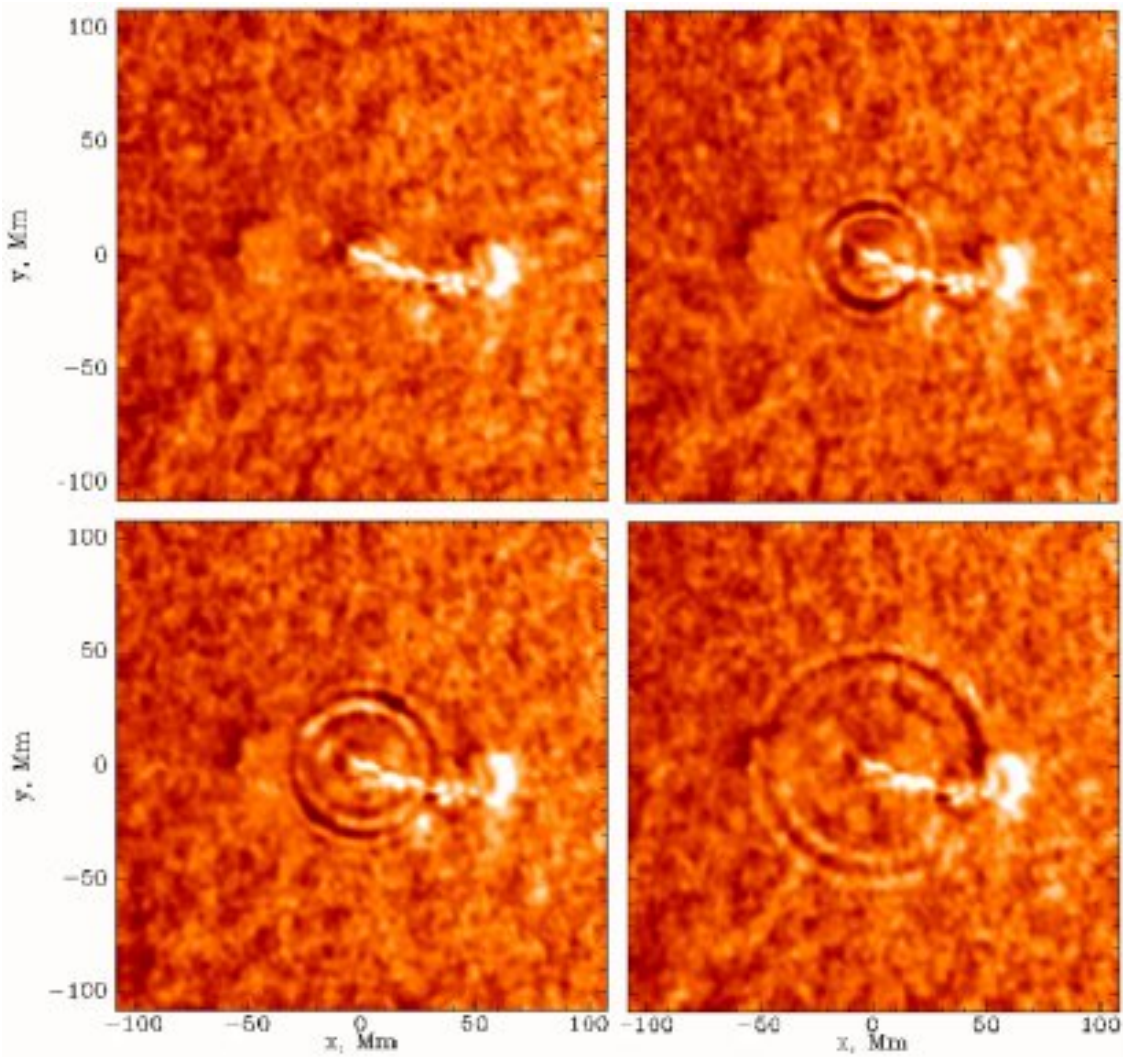


Figure 4: Kosovichev and Zharkova (1998) produced SOHO MDI Dopplergrams from the 1996 July 9th, X class solar flare showing the sunquake expanding outward from it's seismic epicentre to a radial distance of  $1.2 \times 10^8$  metres. Wave-fronts accelerate from a velocity of 30km/s to 100km/s

The first sunquake observation opened up a whole new area of solar physics, leading to subsequent detections associated other flares. The majority of observations show that sunquakes are often the product of highly

impulsive flares, with the acoustic source aligning spatially with white light enhancement in the lower solar atmosphere and hard x-ray emission in the upper-atmosphere (Donea and Lindsey, 2005; Zharkova and Zharkov, 2007). Donea and Lindsey (2005) went on to calculate the energy needed to stimulate the propagation of an acoustic wave in the sub-photosphere, finding that only  $\sim 10^{-3}$  of the energy released by a flare is enough to generate a sunquake. This was an important calculation because it forced the solar community to consider that it might be possible for low energy flares to produce sunquakes, leading to subsequent work by Martínez-Oliveros et al. (2008) looking at seismicity of M-class flares.

A paper by Hudson (2000) put forward for the first time, that sunquake production may depend on the changing configuration of the local magnetic field. This idea was further reinforced by Kosovichev and Zharkova (2001) reporting observations of impulsive changes in magnetic field strength at the photosphere during a solar flare. These magnetic transients were shown to approximately correlate in time and space with hard x-rays, impulsive increases in plasma velocity and increased emission. This line of study was continued (Martínez-Oliveros and Donea, 2009), investigating the magnetic field variation of the photosphere in many flares. The study found that some flares with seismicity do not have a spatial and temporal correlation between sunquakes and magnetic transients. Some flares have magnetic transients and no seismicity, and some flares have a good co-spatial alignment of acoustic activity and magnetic variability. It was noted that the impulsiveness of the magnetic field variation could be important as to whether a sunquake is generated.

Some of the most intriguing of sunquake observations are those that do not abide by the usual set of observable features, in that they are not necessarily associated with hard x-rays and excess white-light emission. For example, a statistical survey carried out by Pedram and Matthews (2012), highlighted a flare containing three footpoints with a seismic source that was co-temporal but not co-spatial with its closest HXR footpoint; and another source which was co-spatial and co-temporal with its nearest HXR footpoint. This showed that a sunquake does not necessarily correlate with locations of peak emission. Another example by Zharkov et al. (2011) reports an observation of two seismic sources associated with footpoints of an erupting flux rope. During the eruption, the magnetic field above each seismic source undergoes an abrupt permanent reconfiguration. The authors cite the possibility that there exists particle beams low enough in population that HXR emission is undetectable. Further papers investigating the same event (Zharkov et al., 2013) show that there are downward motions of material above the seismic sources and that energy provided by magnetic transients may not be able to account for the acoustic power generated. These observational oddities prove that mechanisms that generate sunquakes are not well understood and there is much research to be done to classify the different progenitors.

## 2 Data and Methodology

### 2.1 Observations and Data Reduction

Using data collected by spacecraft observing the Sun, energy released during solar flares can be tracked as it is deposited throughout the atmosphere. The X1 flare of the 29th of March 2014 in active region NOAA 12017, was well observed by RHESSI, IRIS and SDO/HMI, collecting HXR, UV and optical emission respectively. The peak of the impulsive phase of the flare occurs at 17:48 UT, at which point all mentioned instruments provide good coverage. The associated sunquake impact is calculated to have area  $A_{sqk} \sim 2.6 \times 10^{16} \text{ cm}^2$  and power,  $P_{sqk} \sim 1.3 \pm 0.05 \times 10^{26} \text{ erg.s}^{-1}$  (Judge et al., 2014).

#### 2.1.1 The Ramaty High Energy Solar Spectroscopic Imager

The Ramaty High Energy Solar Spectroscopic Imager (RHESSI) observes solar emission ranging from 1 keV X-rays to 20MeV  $\gamma$ -rays produced by energetic particles and nuclear interactions. RHESSI was designed with the aim of understanding impulsive energy release, particle acceleration and transportation in the magnetohydrodynamic environment of the solar atmosphere. Isolating the 10 - 100 keV energy data collected by RHESSI can provide information regarding the intensity and spatial origin of a HXR source. This allows the location of magnetic HXR footpoints to be tracked and the calculation of energy deposition by accelerated electrons.

Once  $P$  has been determined, a total energy can be calculated by multiplying the power by the time period over which the data covers. In this case that would be the impulsive phase of the flare.

Practically applying a thick target model fit to RHESSI data is achieved by using the `ospex` software within SolarSoft (SSWIDL). The entire data set has to be split into short intervals to improve the accuracy of fitting and the detail of resulting plots. The attenuator state of the instrument has to be taken into account due to differences in sensitivity to incoming photons. Therefore it is important to define intervals for fitting first by the attenuator state as `ospex` will mitigate for the differences in count sensitivity. Then each attenuator time period can be split further in to smaller time increments.

Shown in Figure 6 is the resulting fit over the impulsive phase of the flare. At the peak of the impulsive phase between 17:46 and 17:48 the RHESSI fit shows an energy ranging from  $1.0 \times 10^{28}$  to  $2.5 \times 10^{29}$  erg. Assuming the fitting model is correct then the release of this energy is due to non-thermal electrons being accelerated by magnetic reconnection, depositing their energy into the chromosphere.

#### 2.1.2 The Interface Region Imaging Spectrograph

Observing UV ribbons requires a different spacecraft. The Interface Region Spectroscopic Imager (IRIS) captures near-ultraviolet (NUV) and far-ultraviolet (FUV) emission and is designed to observe the chromosphere at various altitudes. Emission is collected by a slit-jaw imager (SJI) and a spectrometer (SG) simultaneously. The spectrograph is sensitive in both FUV and NUV passbands, which expose 3 CCDs to produce spectra in three UV bands, two FUV and one NUV. Table 2 shows how each passband relates to emission processes occurring from the upper-chromosphere down to the upper-photosphere.

Band	Wavelength Å	Temperature log $T$	Region of Atmosphere
FUV 1	1331.7 – 1358.4	3.7 – 7.0	Upper to lower-chromosphere
FUV 2	1389.0 – 1407.0	3.7 – 5.2	Upper to lower-chromosphere
NUV	2782.7 – 2851.1	3.7 – 4.2	Chromosphere to upper-photosphere

Table 2: The IRIS/SG is capable of observing three passbands, which relate to different plasma temperatures.

The slit-jaw images, are light collected from a reflective area surrounding the slit. The imager is capable of observing four wavelengths relating to emission at different altitudes as shown by Table 3.

SJI Passband	Wavelength Å	FWHM Å	Temperature log $T$	Region of Atmosphere
C II	1330	40	3.7 – 7.0	Upper-chromosphere
Si IV	1400	40	3.7 – 5.2	Upper-chromosphere
Mg II h/k	2796	4	3.7 – 4.2	Lower-chromosphere
Mg II wing	2832	4	3.7 – 3.8	Upper-photosphere

Table 3: The IRIS/SJ is capable of observing four passbands, which relate to different plasma temperatures.



The IRIS spacecraft captured the temporal evolution of the flare between 14:09 and 17:54 UT via its slit-jaw imager and spectrograph at solar coordinates 491", 282", with a spatial resolution of 0.1667" per pixel. The slit-jaw imager data provides coverage of a field of view spanning 167" by 174", of passbands that including 1403, 2796 and 2832 Å at 26, 19 and 75 second cadence respectively. The spectrograph slit has a field of view spanning 14" by 174" and is aligned directly over chromospheric flare ribbons, and the sunquake point of origin. For the majority of the observation, the spectrograph slit is exposed for  $\sim 9$  seconds at 8 slit locations for a total of 72 seconds cadence per raster. However, during the impulsive phase the IRIS SG shortens its exposure time to around 2.4 seconds in order to mitigate against saturation of the CCDs. Wavelengths observed over three channels include FUV1: 1331.7 - 1358.4 Å, FUV2: 1389.0 - 1407.0 Å and NUV: 2782.7 - 2851.1 Å, associated with the transition region, chromosphere and the upper-photosphere. Spectral lines include C II, Si IV and Mg II h and k. IRIS SJI data is the standard level 2 data product provided for scientific research, which has been calibrated to negate dark currents, flat-field and spacecraft rotational effects. In order to observe flare ribbons in the photospheric data captured by IRIS SJI MG II wing channel, a running difference filter is applied. This effectively removes unwanted background features, highlighting the UV ribbons. IRIS SG data is manually corrected for changing exposure times and wavelength shifts caused by the orbital motions of the spacecraft. IRIS SG data is sampled over a wavelength range of 2825.7 and 2825.8 Å which represents a sample of Balmer pseudo-continuum. The next stage of the processing requires that IRIS SJ and SG data are converted from relative intensity (DN per pixel) to energy (erg) units. This is achieved by using a method provided in the instrument documentation (De Pontieu et al., 2014) which calculates the conversion factors between DN and erg units in SSWIDL. It is then a case of inserting IRIS DN per pixel intensity values into the equation 18 converting them into energy units.  $F_{DN}$  is flux in units of DN per pixel,  $C_{d2p}$  is the DN to photon conversion factor,  $E_\lambda$  is the photon energy and  $E_{erg}$  is to put the result into erg units.

$$E = \frac{F_{DN} C_{d2p} E_\lambda}{E_{erg}} \quad (18)$$

### 2.1.3 The Solar Dynamics Observatory's Helioseismic and Magnetic Imager

Signatures of energy deposition in the lowest regions of atmosphere are captured by Solar Dynamics Observatory's (SDO) Helioseismic Imager (HMI), which is sensitive to the wing of the photospheric absorption line 6173 Å (Fe I), which is essentially optical continuum. SDO/HMI has three main observables, continuum, dopplergrams and magnetic field configuration, each of which can provide valuable insight into the physical conditions existing in photospheric plasma. In particular for this project, optical continuum data can provide information about WLFs intensity, which along with Balmer continuum could be linked to radiative backwarming of photospheric material, which is a possible sunquake progenitor. The point of origin and wave-fronts of the sunquake can also be detected using helioseismic data, which can be used to calculate acoustic power of the quake. The HMI instrument onboard SDO observes the entire solar photosphere with 4k resolution and a pixel size relating to 0.505" by 0.505", with each image having a cadence of 45 seconds. The data is calibrated to negate cosmic-rays, dark currents, flat-field and spacecraft rotational effects. In this project, HMI continuum data is used primarily to observe White light flares, which are difficult to see against the bright photospheric background. To highlight the positions of flare ribbons in the photosphere, data must be filtered. Similarly to Kerr and Fletcher (2014), photospheric continuum data captured by HMI is put through a two stage filtering procedure. First the data has an unsharp filter applied, so that the filtered image,  $I_{filt} = I - \text{smooth}(I, 10)$ , where  $I$  is the original image and the function smooth relates to a 10 pixel boxcar smoothing filter, this is to remove small features such as granulation. The technique is not perfect meaning that some granulation is still visible after the unsharp filter. Second,  $I_{filt}$  is subjected to a running difference filter to isolate locations that are white-light enhanced. The running difference filter effectively removes static features leaving behind those pixels that are changing over short time-scales. However, for removing signatures of those processes occurring over shorter time periods such as the remaining granulation and also p-mode oscillations, this filtering technique is ineffective. This is not a problem, as for the purpose of white light flare analysis, the data yield a strong contrast between flare-enhanced and background pixels after being filtered by a  $i - 2$  running difference. The next stage is to determine which pixels in the difference image are those that are enhanced during the flare. For the best result, white-light enhanced pixels are identified using a combination of visual inspection and thresholding. Attempts at automating the identification process tend to lead to false positives being triggered by noise or granulation features.

HMI Dopplergrams are used in conjunction with holography techniques to produce a 6mHZ acoustic egression power map (supplied via private communication by Sergei Zharkov) revealing the location of the sunquake. As



Sample Number	Heliocentric Position (x,y)
1	518.219", 262.000"
2	520.215", 263.000"
3	522.212", 262.000"
4	522.212", 265.000"
5	524.256", 265.000"
6	526.252", 263.818"

Table 4: Sample number and the corresponding coordinates in heliocentric units (arcsec).

with the IRIS data, the next stage of processing is to calculate and energy. To perform the energy conversion for SDO HMI data a combination of sources (Boerner et al., 2012; Couvidat et al., 2012) have been used to find the instrument’s properties which are used to fulfil a conversion factor in the form of equation 19. Where  $g$  is the instrument gain,  $QE$  is the quantum efficiency of the charged couple device and  $A_{ap}$  is the instrument aperture area, all other terms hold the same meaning as in equation 18.

$$E = \frac{F_{DN}E_{\lambda}}{gQE A_{ap}E_{erg}} \quad (19)$$

## 2.2 Data Sampling

For the IRIS SJI, IRIS SG and SDO HMI data sets, multiple sample points have been chosen based on the moment in time when the IRIS SG slit is directly over the southern flare ribbon and sunquake impact location. These coordinates are sampled across all data sets except RHESSI due to the limited spatial resolution of the instrument. Figure 5 shows the sample coordinates, RHESSI HXR and the 6mHz sunquake egression map, plotted over filtered SDO HMI data in an effort to demonstrate the spatial alignment between HXR (particle beam), UV ribbons and sunquake impact. Table 4 shows how each sample number relates to a heliocentric position in arcseconds.

Figure 5: The images show IRIS Mg II slit-jaw data with contours representing HXR emission and 6mHz sunquake power. The black box highlights the area contained in the zoomed plot on the right. The cyan contours show the 6mHz egression power, with the location of the sunquake shown in red on the right. The green and red contours on the left plot show RHESSI HXR data at 25 - 50 and 50 - 100 keV. The green crosses on the right plot show sample positions numbered in accordance with table 4 Each of the IRIS SJ and SDO HMI data sets are sampled at the exact same coordinates in heliocentric units.

### 3 Results and Discussion

#### 3.1 RHESSI Hard X-rays

For a sunquake to be generated by accelerated particle collision then the incident beam must be aligned over the acoustic impact location (). To highlight this spatial alignment, RHESSI 50 to 100 keV HXR and sunquake egression power contours are plotted on a reverse colour, filtered HMI continuum image shown in figure 5. The contours show a reasonable alignment but a more rigorous way to test the spatial and temporal relationship between HXR, sunquake and other emission is to analyse lightcurves from the region of interest.

RHESSI HXR data is taken from central coordinates 518" by 262", sampling the sunquake epicenter. When this data is fit to a nonthermal electron model a spectrum is produced, which can be used to plot the energy curve shown in Figure 6. The plot shows 10 - 100 keV HXR power as a function of time. The impulsive phase of the flare is visible from 17:46, peaking at 17:47, with the plot showing a double peak profile which climbs from  $1.0 \times 10^{28}$  to  $2.5 \times 10^{29}$  erg.

To put this in the context of the associated sunquake, the HXR energy can be used to estimate the amount of energy provided to the acoustic impact area, or nonthermal flux via

$$F_e = \frac{P_e}{A_{HXR}} \quad (20)$$

where flux  $F_e$  is in units of  $\text{erg.s}^{-1}.\text{cm}^{-2}$ ,  $P_e$  is nonthermal power and the HXR emission area is  $A_{HXR} \sim \dots$ . The resulting flux can be multiplied by the sunquake area, to determine an upper limit for the nonthermal power available for generating an acoustic disturbance  $P_e(A_{sqk}) = F_e \times A_{sqk}$ . So with  $P_e \sim 10^{29} \text{ erg.s}^{-1}$ ,  $P_e(A_{sqk}) = \dots$ . Comparing this value to the sunquake power  $P_{sqk} \sim 1.3 \pm 0.05 \times 10^{26} \text{ erg.s}^{-1}$  it is clear that the electron beam does/doesnot have the energy to cause the sunquake. Another interesting quantity to investigate is the momentum of the particle beam. Electron momentum can be calculated by

$$p_e = \tau \sqrt{2m_e P_e} \quad (21)$$

where  $m_e$  is electron mass,  $\tau$  is the time duration of flare impulsive phase and  $P_e$  is described by equation 12. Substituting values in to equation 3.1 yields an electron momentum of  $p_e \sim 1.35 \times 10^{17} \text{ g cm s}^{-1}$ . Assuming the energy in the electron beam is equal to that in a population of accelerated protons, then calculation of a theoretical proton beam momentum, where  $m_p$  is the proton mass, is by the relation,

$$p_p \sim p_e \sqrt{\frac{m_p}{m_e}} \quad (22)$$

Which yields a proton momentum of  $p_p \sim 5.79 \times 10^{18} \text{ g cm s}^{-1}$ , an order of magnitude greater than  $p_e$ . This is because  $m_p = 2000m_e$  meaning the square root in equation 3.1 renders the result  $p_p \sim 44.7p_e$ . So in order to determine whether a particle beam carries enough momentum to stimulate a sunquake, a calculation of the momentum needed to initiated the acoustic response is required.

The momentum needed to produce the sunquake is

$$p_{sqk} \sim \rho l^3 v \quad (23)$$

where all terms are tailored for photospheric values, hence density  $\rho \sim 10\text{--}8 \text{ g cm}^{-3}$ ; sound speed  $v \sim 10^6 \text{ cm.s}^{-1}$ . The length-scale,  $l \sim 1.82 \times 10^8$ , corresponds to the sunquake impact diameter,

$$l = 2 \sqrt{\frac{A_{sqk}}{\pi}} \quad (24)$$

Equation 3.1 gives the momentum of the acoustic reponse as  $p_{sqk} = 6.03 \times 10^{22} \text{ g cm s}^{-1}$ , which when compared to particle beam momenta,  $p_e$  and  $p_p$ , is 105 and  $10^4$  times larger respectively. This means that even if an electron or proton beam can make it down to the photosphere, it wouldn't have the necessary momentum to cause the sunquake on it's own. In reality, calculated momenta are idealistic, not treating the effects of energy loss due to energy dissipation. The point being that for a particle beam to make it to the photosphere,

it has to traverse 9 pressure scale heights, increasing in density with depth. As density increases particles in the beam are more likely to encounter ambient plasma, and as a result are decelerated, giving up as energy as emission. So if or when the beam reaches the photosphere, much of its energy and momentum has already been dissipated in the chromosphere, making the generation of a sunquake via just the particle beam even more unlikely.

### RHESSI 10 - 100 keV Hard Xray Energy Over Time

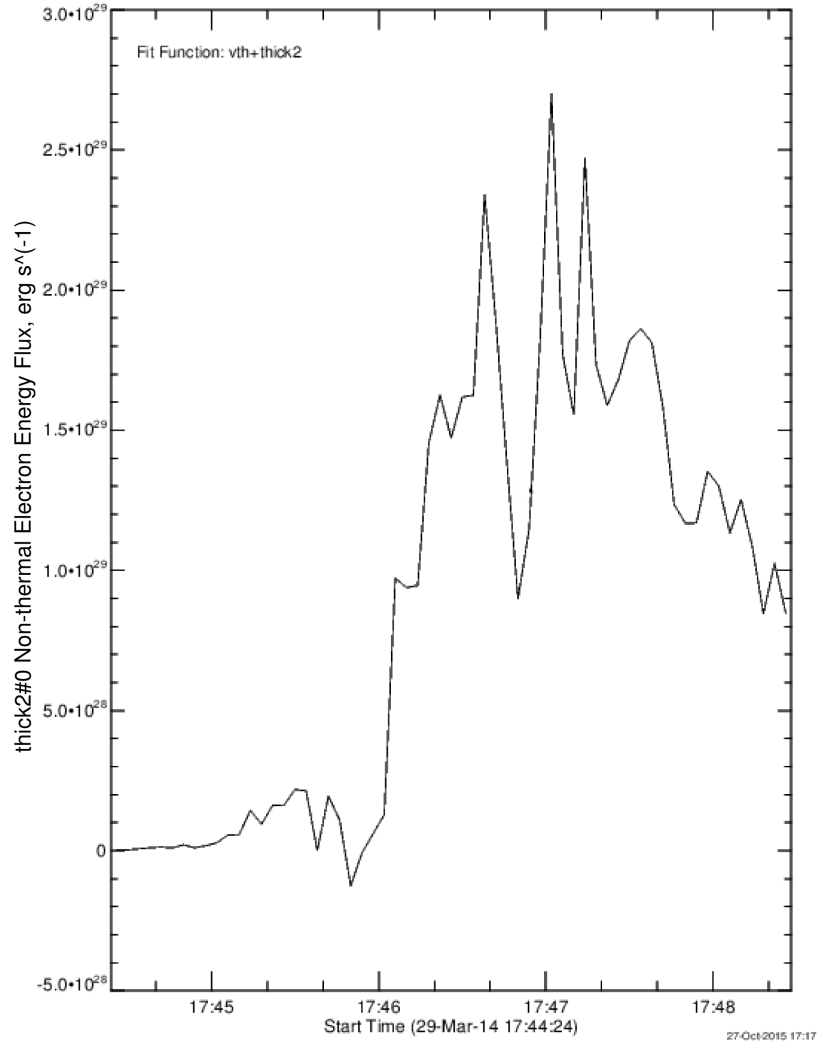


Figure 6: Shows the energy evolution of hard x-ray emission collected by RHESSI 10 to 100 keV bins over the sunquake region (518'', 262''). HXR emission is due to non-thermal electrons, thus energy is calculated by fitting data to the collisional thick target model. The HXRs impulsive phase begins at around 17:46 and peaks at 17:47, showing temporal alignment with IRIS and HMI datasets shown in Figure 7

### 3.2 Emission Captured By IRIS and HMI

However, energy deposited into the atmosphere by the particle beam can lead to other sunquake generation mechanisms, such as radiative backwarming and shocks which are described in sections 1.4.1.A recent result from shows that the intensity of Balmer continuum observed in this event could come from either; 23of < 20 keV nonthermal electrons; or the entire population of < 40 keV momthermal electrons. This means that a large portion of energy delivered to the lower atmosphere by the electron beam is dissipated causing various continua and emission lines. Shown in Figure 7 are lightcurves of emission from the lower solar atmosphere, captured by IRIS and SDO HMI. From top to bottom the plot shows data from IRIS SJ Si IV, IRIS SJ Mg II, IRIS SG Balmer Continuum, IRIS SJ Mg II wing and SDO HMI visible continuum sampled from six coordinates in the flare ribbon. Si IV and Mg II IRIS SJ data, show a distinct cutoff which is caused by over saturation of the instrument CCD, meaning flux measurements during the impulsive phase are a lower estimate. However, Si IV

and Mg II lightcurves can still be used to confirm temporal and spatial alignment of energy deposition at these wavelengths. All coordinates in all datasets show a synchronised impulsive peak, with the exception of MG II wing where only coordinates four and five exhibit a significant enhancement. The red solid line in each data set is sampled from the sunquake location. At first glance the sunquake location in the plots does not seem to have any obvious differences other than a slight time delay in peak balmer continuum emission. The delay appears to be around 45 seconds after the impulsive phase peak at approximately 17:48 which coincides with the sunquake onset time????????? Mg II wing data shows no enhancement over the sunquake location. HMI continuum shows significant enhancement over the sunquake, which is aligned in time with the impulsive phase.

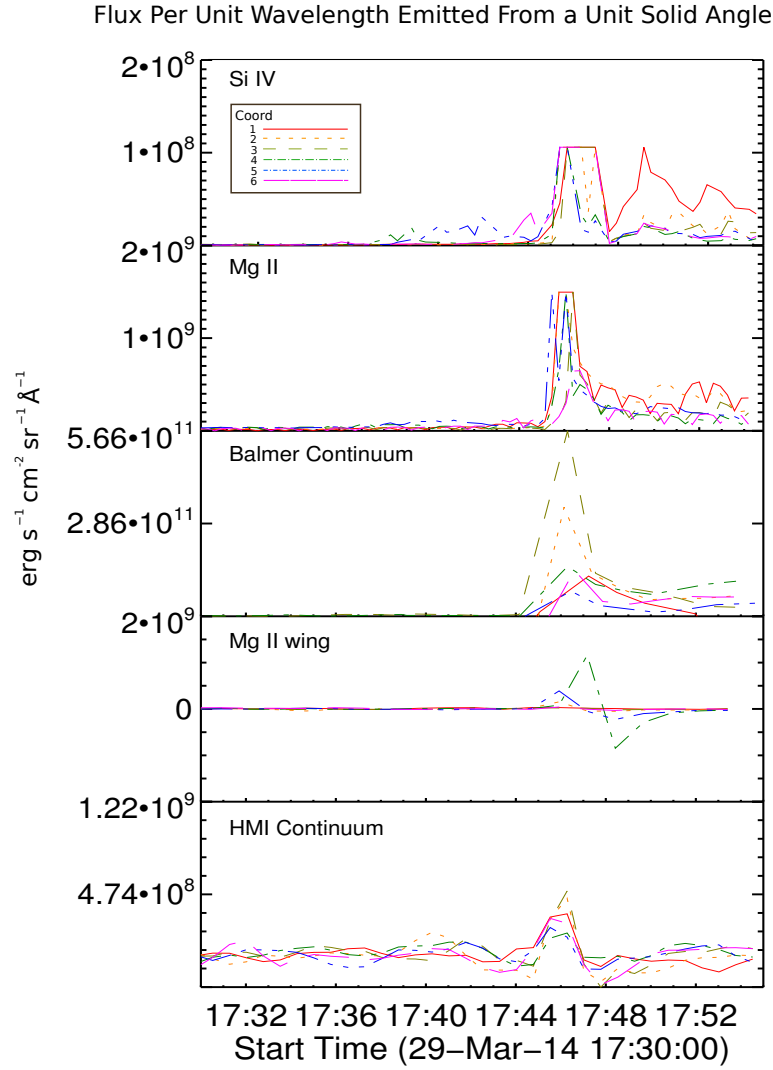


Figure 7: Shows flux per wavelength from a unit solid angle [ $\text{erg.s}^{-1}.\text{sr}^{-1}.\text{\AA}^{-1}$ ]. The six lines (see legend) represent areas centered on regions 1 to 6, relating to heliocentric coordinates shown in Table 4. The solid red line is directly over the sunquake location. Each plot represents an independant data set, in order from top to bottom the sets are; IRIS SJ 1400 (Si IV); IRIS SJ 2796 (Mg II); IRIS SG 2825.7 to 2825.8 (Balmer Continuum); IRIS SJ 2832 (Mg II wing); SDO HMI continuum (HMI).

Balmer continuum enhancement is in angreement with 1D... models by

HMI shows an enhancement of ... which is similar to values claculated by . This means that the novel energy conversion method employed in the data reduction produces a reliable result.

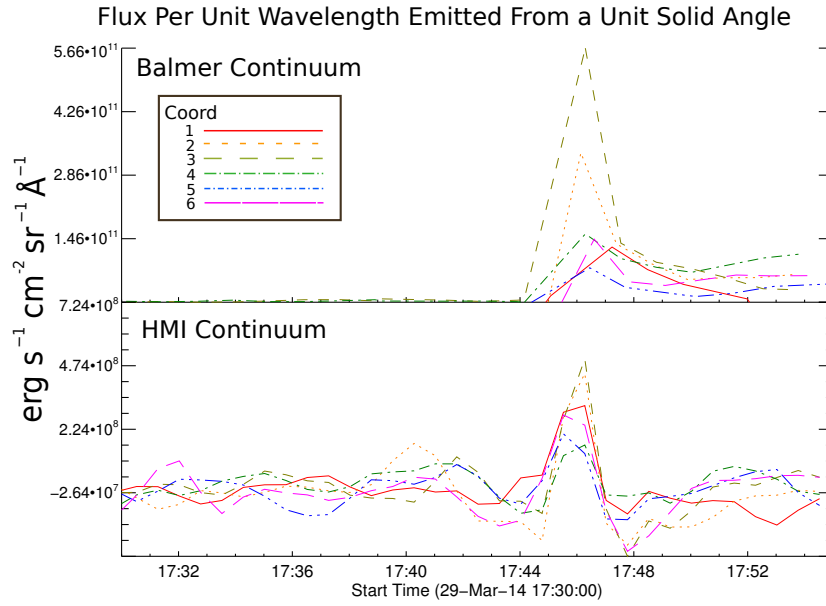


Figure 8: Shows flux per wavelength from a unit solid angle [ $\text{erg.s}^{-1}.\text{sr}^{-1}.\text{\AA}^{-1}$ ]. The six lines (see legend) represent areas centered on regions 1 to 6, relating to heliocentric coordinates shown in Table 4. The solid red line is directly over the sunquake location. Each plot represents an independent data set, in order from top to bottom the sets are; IRIS SJ 1400 (Si IV); IRIS SJ 2796 (Mg II); IRIS SG 2825.7 to 2825.8 (Balmer Continuum); IRIS SJ 2832 (Mg II wing); SDO HMI continuum (HMI).

The flux values for Balmer and HMI continuum shown in Figure 8 can be used to estimate the power of the radiative backwarming. The key being whether the radiative backwarming is powerful enough to generate the sunquake. The power profiles shown in Figure 10 are calculated by assuming a homogenous energy distribution in the region surrounding each coordinate, it is then possible to use the relation,

$$P_{\text{Balm}} = F_{\text{Balm}} \times A_{\text{sqk}} \quad (25)$$

where  $P_{\text{Balm}}$  is the power of the Balmer continuum emitted from an area equal to the sunquake,  $A_{\text{sqk}}$ . The same data set and coordinate scheme is followed as in Figure 8. The Balmer continuum over the sunquake shows an impulsive power  $P_{\text{Balm}} = 6 \times 10^{13} \text{ erg.s}^{-1}$  which is thirteen orders of magnitude smaller than the power of the sunquake  $P_{\text{sqk}} \sim 1.3 \pm 0.05 \times 10^{26} \text{ erg.s}^{-1}$ . This means that there is not enough energy per second deposited by radiative backwarming to create the sunquake. The HMI continuum power,  $P_{\text{HMI}}$ , over the sunquake location peaks at  $P_{\text{HMI}} = 2 \times 10^{14} \text{ erg.s}^{-1} \text{ cm}^{-2}$ , which is twelve orders of magnitude less than the  $P_{\text{sqk}}$ .

The Balmer and HMI continuum displayed in Figure 10

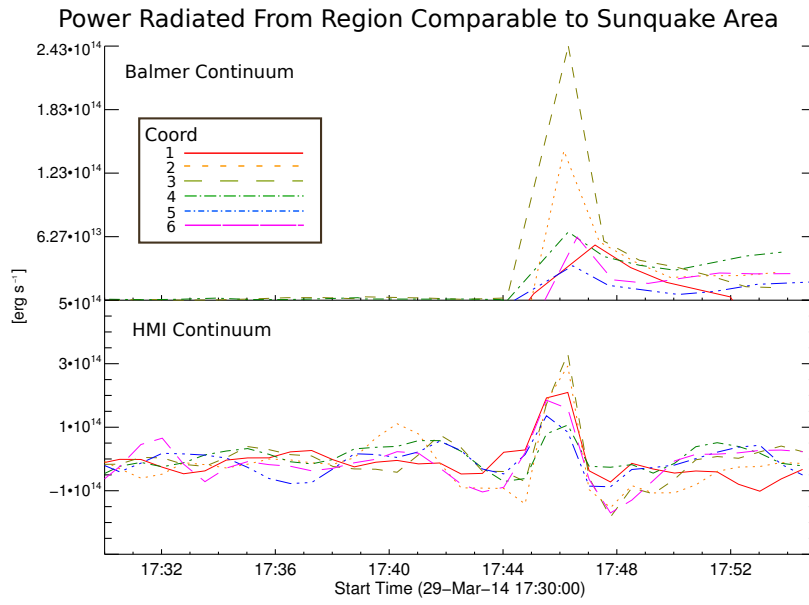


Figure 9: Shows radiative power [erg.s<sup>-1</sup>], which is the result of flux data that has been multiplied by the sunquake impact area. The six lines (see legend) represent areas centered on regions 1 to 6, relating to heliocentric coordinates shown in Table 4. The solid red line is directly over the sunquake location. The top plot is IRIS SG 2825.7 to 2825.8 Balmer Continuum and the bottom plot is SDO HMI continuum.

Integrating radiative flux over the impulsive phase of the flare provides an upper limit for energy deposited in the lower atmosphere. With the exception of Si IV and Mg II data, which are over saturated and so level off at a lower flux, rendering a lower energy deposition limit. The integrated flux is calculated,

$$F_{imp} = \int_0^\tau F(t)dt = E(t)\tau \quad (26)$$

where the duration of the impulsive phase  $\tau =$  and  $F(t)$  is the emitted flux at time  $t$ .

$F_{imp}$  can be used to estimate the radiative energy emitted from an area comparable to  $A_{sqk}$  as,

$$E_{imp} = F_{imp} \times A_{sqk} \quad (27)$$

where it is assumed that a homogenous energy distribution exists throughout the sunquake impact area. This produces values for each data set tabulated in Table 5.

Si IV

Mg II

Balmer continuum

Mg II wing

HMI continuum

Coord Number	Coordinates (x,y) [arcsecs]	$E_{S,IV}$ [erg]	$E_{MgII}$ [erg]	$E_{Bal,m}$ [erg]	$E_{MgIw}$ [erg]	$E_{HMI}$ [erg]
1	518.22, 262.00	6.74E+12	1.41E+14	5.98E+15	4.27E+12	1.42E+16
2	520.22, 263.00	5.65E+12	1.35E+14	1.71E+16	7.14E+12	1.10E+15
3	522.21, 262.00	5.18E+12	7.83E+13	2.52E+16	2.91E+12	4.82E+15
4	522.21, 265.00	3.93E+12	8.35E+13	9.89E+15	6.70E+13	1.28E+15
5	524.26, 265.00	3.98E+12	1.03E+14	4.37E+15	1.86E+13	8.99E+14
6	526.25, 263.82	6.91E+12	6.34E+13	5.24E+15	1.74E+12	9.88E+14

Table 5: Flux integrated over the flare impulsive phase (17:44 to 17:48) is then multiplied by the sunquake impact area to produce a total deposited energy. The values show are for ribbon sample locations 1 to 6.

## 4 Interpretation and Discussion

The spatial and temporal alignment of 10 to 100 keV HXR and emission from lower altitudes (Figure ??) is further backed up by . They show that peak emission during the flare from various continua are in good alignment in space and time with the 30 to 100 keV HXR source.

suggest that the stimulation of a sunquake by direct particle beam interaction is caused by an injection of electrons aligned with the acoustic impact location. For this reason, the electron beam in the 29th of March flare is a candidate progenitor of the observed sunquake.

However, further analysis has shown that the momentum carried the electron beam is insufficient to generate the quake. Furthermore the derived proton beam momentum also falls short, meaning that the sunquake is not generated by particle beam collision.

$p_{sqk}$  is at least three orders of magnitude higher than electron and proton beam momenta  $p_e$  and  $p_p$ . This means that direct particle collision is unlikely to be causing the sunquake.

So what is causing the sunquake?

shocks? ? show that there is substantial redshifted spectral lines during the impulsive phase that indicate the existence of shocks.

Dissipation of Alfvén waves? ? mentioned by ? as a possible energy transport mechanism maybe capable of producing a sunquake.

Lorentz force? Judge et al. (2014) show that the Lorentz force is



## 5 Conclusions and Thesis Plan

As inferred from 50 to 100 keV HXR measurements, the impulsive phase of the flare occurs from 17:46 to 17:47. HXR contours and energy curve show that there is a nonthermal electron beam directly over the sunquake.

The electron beam has/hasn't enough energy to cause the sunquake.

Even with the most idealistic of circumstances, the electron beam momentum of  $p_e \sim 1.35 \times 10^{17} \text{ g cm s}^{-1}$  is ... orders of magnitude smaller than that required to produce the sunquake. It is a similar conclusion for the theoretical proton beam momentum of ..., which is ??? times smaller than  $p_{sqk}$ .

For these reasons it is unlikely that a nonthermal particle beam is capable of producing a sunquake in this event.

Although there seems to be some radiative backwarming occurring, it is evident from time integrated flux calculations of the Balmer continuum emission that there is insufficient radiative energy to generate the sunquake.

# Appendices

## A Equations

**Maxwell's Equations and Ohm's Law** Maxwell's equations and Ohm's law describe electromagnetism in terms of magnetic induction  $\mathbf{B}$ , magnetic permeability of free space  $\mu$ , electric field  $\mathbf{E}$ , electrical permittivity of free space  $\epsilon_0$ , charge density  $\rho_c$  and electric current density  $\mathbf{j}$

### Ampere's Law

$$\nabla \times \mathbf{B} = \mu_0(\mathbf{j} + \epsilon_0 \frac{\partial \mathbf{E}}{\partial t}) \quad (28)$$

### Faraday's Law

$$\nabla \times \mathbf{E} = -\frac{\partial \mathbf{B}}{\partial t} \quad (29)$$

### Gauss's Law

$$\nabla \cdot \mathbf{E} = \frac{\rho_c}{\epsilon_0} \quad (30)$$

### No Magnetic Monopoles

$$\nabla \cdot \mathbf{B} = 0 \quad (31)$$

with Ohm's law as,

$$\mathbf{j} = \sigma(\mathbf{E} + \mathbf{v} \times \mathbf{B}) \quad (32)$$

where  $\sigma$  is electrical conductivity.

**Fluid Dynamics Equations** The fluid dynamics relations are written in terms of density  $\rho$ , velocity  $\mathbf{v}$ , time  $t$ , pressure  $p$ , gas constant  $\Re$  and temperature  $T$ .

$$\rho \frac{d\mathbf{v}}{dt} = -\nabla p \quad (33)$$

$$\frac{d\rho}{dt} + \rho \nabla \cdot \mathbf{v} = 0 \quad (34)$$

$$p = \Re \rho T \quad (35)$$

Equation 32 is the eqn. of motion describing how the forces are exerted on the fluid are equal to the negative gradient of plasma pressure. Equation 33 is the eqn. of mass continuity (mass is conserved), whilst equation 34 is the perfect gas law relating plasma pressure, density and temperature.

**MHD Equations** Another way to write the relationship between  $\mathbf{B}$  and  $\mathbf{v}$  is the equation of motion 32 modified by the Lorentz force.

$$\rho \frac{d\mathbf{v}}{dt} = -\nabla p + \mathbf{j} \times \mathbf{B} \quad (36)$$

The pressure gradient  $-\nabla p$  describes the change from high to low plasma pressure. The Lorentz force,  $\mathbf{j} \times \mathbf{B}$  acts perpendicularly to the magnetic field, therefore accelerated plasma in a direction parallel to the magnetic field is caused by other forces. If equation ?? is substituted into the Lorentz force,

$$\mathbf{j} \times \mathbf{B} = (\nabla \times \frac{\mathbf{B}}{\mu}) \times \mathbf{B} \quad (37)$$

$$\rho \frac{d\mathbf{v}}{dt} = -\nabla p + (\mathbf{B} \cdot \nabla) \frac{\mathbf{B}}{\mu} - \nabla(\frac{B^2}{2\mu}) \quad (38)$$

Because  $-\nabla(\frac{B^2}{2\mu})$  is in the same form as  $-\nabla p$  it can be said to be the *magnetic pressure*, providing a force pointing from high to low magnetic pressure as  $B^2$  changes with position.

## Reduced MHD Equations Based on assumptions:

- $v \ll v_c$ , typical plasma velocities are much slower than the sound speed
- All the effects of radiation, viscosity, electric charge density and displacement currents are negligible

It is possible to reduce Maxwell's equations into the following form:

### Ampere's Law

$$\nabla \times \mathbf{B} = \mu_0 \mathbf{j} \quad (39)$$

### Faraday's Law

$$\nabla \times \mathbf{E} = -\frac{\partial \mathbf{B}}{\partial t} \quad (40)$$

### Gauss's Law

$$\nabla \cdot \mathbf{E} = 0 \quad (41)$$

### No Magnetic Monopoles

$$\nabla \cdot \mathbf{B} = 0 \quad (42)$$

## B Figures

Power Radiated Over Sunquake Area (Central Coords 518.22", 262.00")

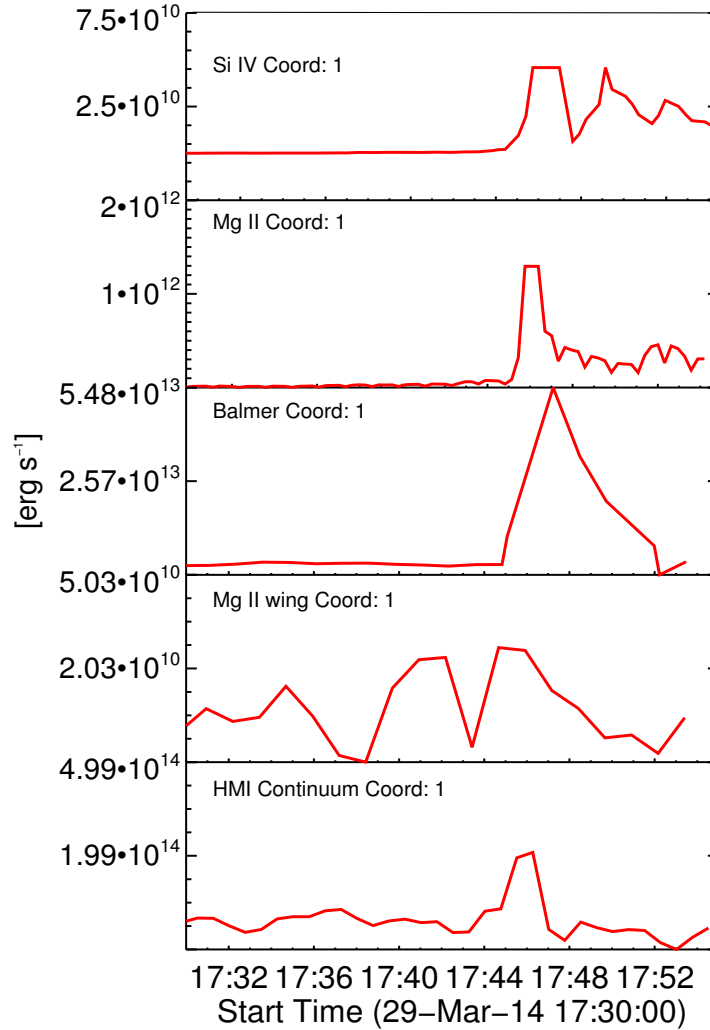


Figure 10: Shows radiative power from an area comparable to the sunquake impact, centered on region 1, relating to heliocentric coordinates 518.2", 262.0" which is directly over the sunquake location. Each plot represents an independent data set, in order from top to bottom the sets are; IRIS SJ 1400 Å (Si IV); IRIS SJ 2796 Å (Mg II); IRIS SG 2825.7 to 2825.8 Å (Balmer Continuum); IRIS SJ 2832 Å (Mg II wing); SDO HMI continuum (HMI).

## Quake Location Energy Over Time

Power Radiated Over Sunquake Area (Central Coords 520.22", 263.00")

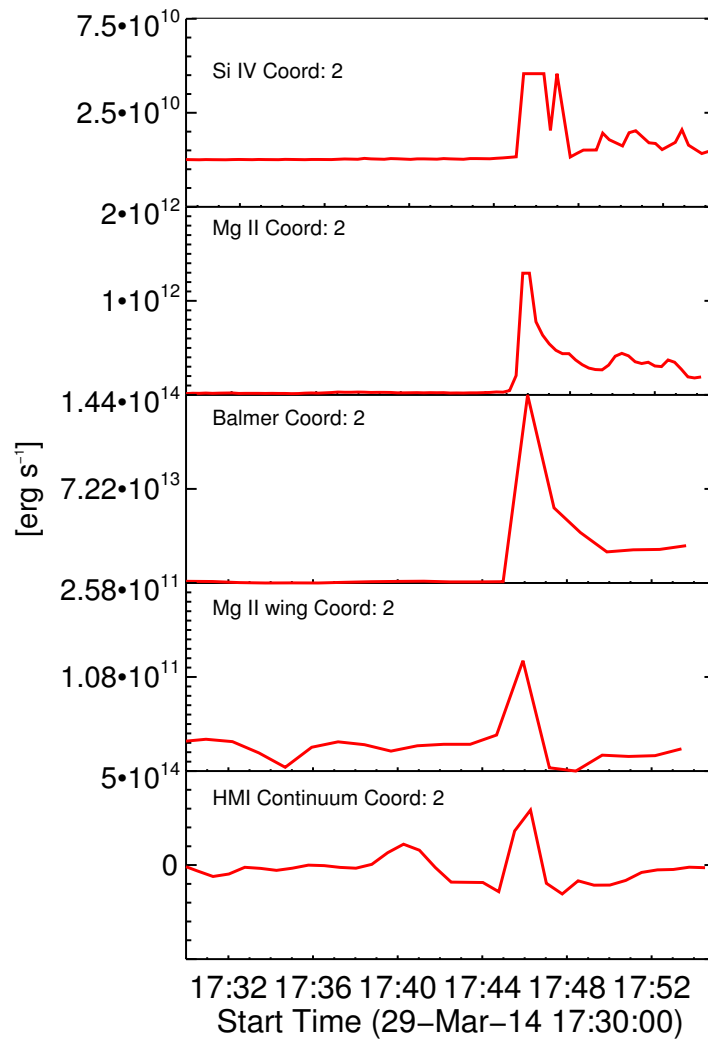


Figure 11: Shows radiative power from an area comparable to the sunquake impact, centered on region 2, which relates to heliocentric coordinates 520.2", 263.0". Each plot represents an independant data set, in order from top to bottom the sets are; IRIS SJ 1400 Å (Si IV); IRIS SJ 2796 Å (Mg II); IRIS SG 2825.7 to 2825.8 Å (Balmer Continuum); IRIS SJ 2832 Å (Mg II wing); SDO HMI continuum (HMI).

**Quake Location Energy Over Time**  
 Power Radiated Over Sunquake Area (Central Coords 522.21",262.00")

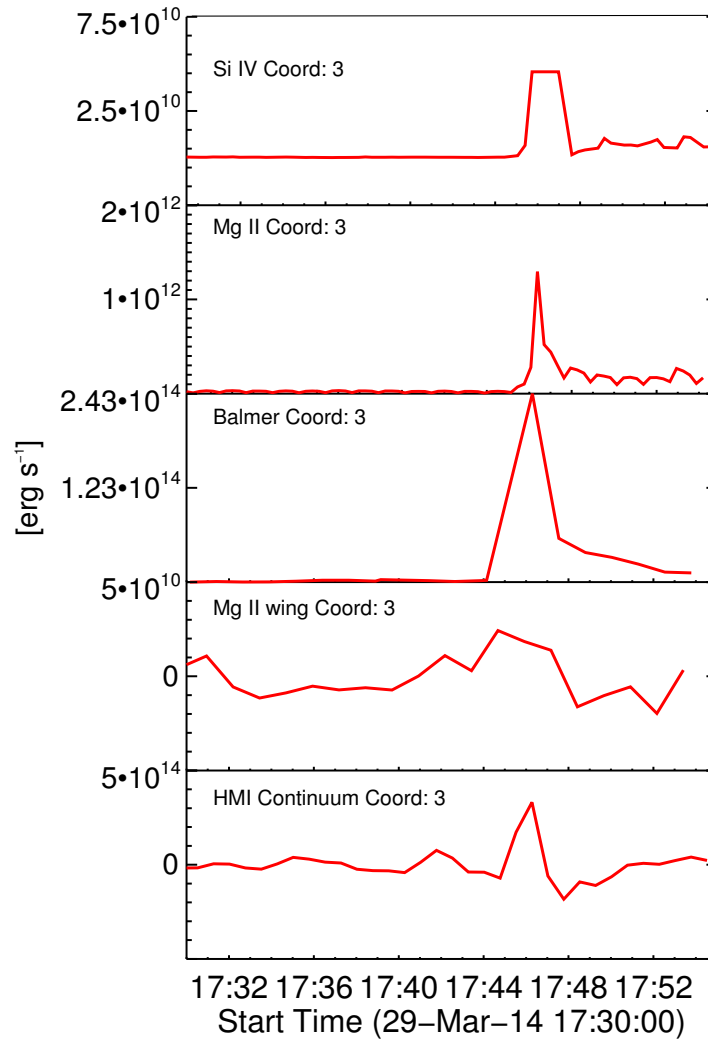


Figure 12: Shows radiative power from an area comparable to the sunquake impact, centered on region 3, which relates to heliocentric coordinates 522.2", 262.0". Each plot represents an independant data set, in order from top to bottom the sets are; IRIS SJ 1400 Å (Si IV); IRIS SJ 2796 Å (Mg II); IRIS SG 2825.7 to 2825.8 Å (Balmer Continuum); IRIS SJ 2832 Å (Mg II wing); SDO HMI continuum (HMI).

## Quake Location Energy Over Time

Power Radiated Over Sunquake Area (Central Coords 522.21", 265.00")

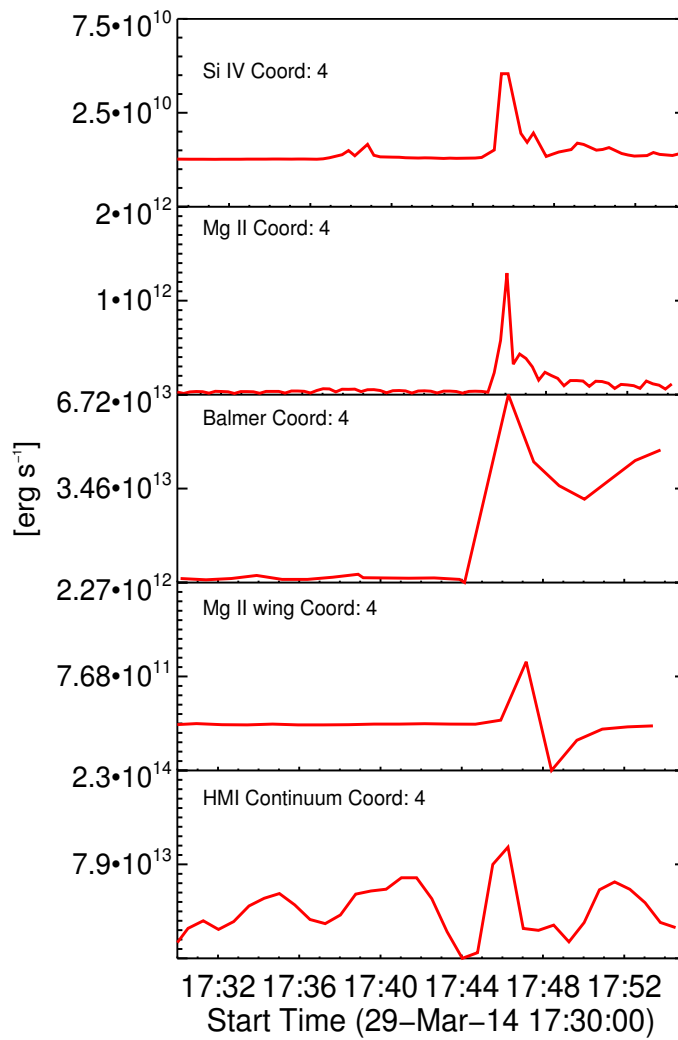


Figure 13: Shows radiative power from an area comparable to the sunquake impact, centered on region 4, which relates to heliocentric coordinates 522.2", 265.0". Each plot represents an independant data set, in order from top to bottom the sets are; IRIS SJ 1400 Å (Si IV); IRIS SJ 2796 Å (Mg II); IRIS SG 2825.7 to 2825.8 Å (Balmer Continuum); IRIS SJ 2832 Å (Mg II wing); SDO HMI continuum (HMI).

## Quake Location Energy Over Time

Power Radiated Over Sunquake Area (Central Coords 524.26", 265.00")

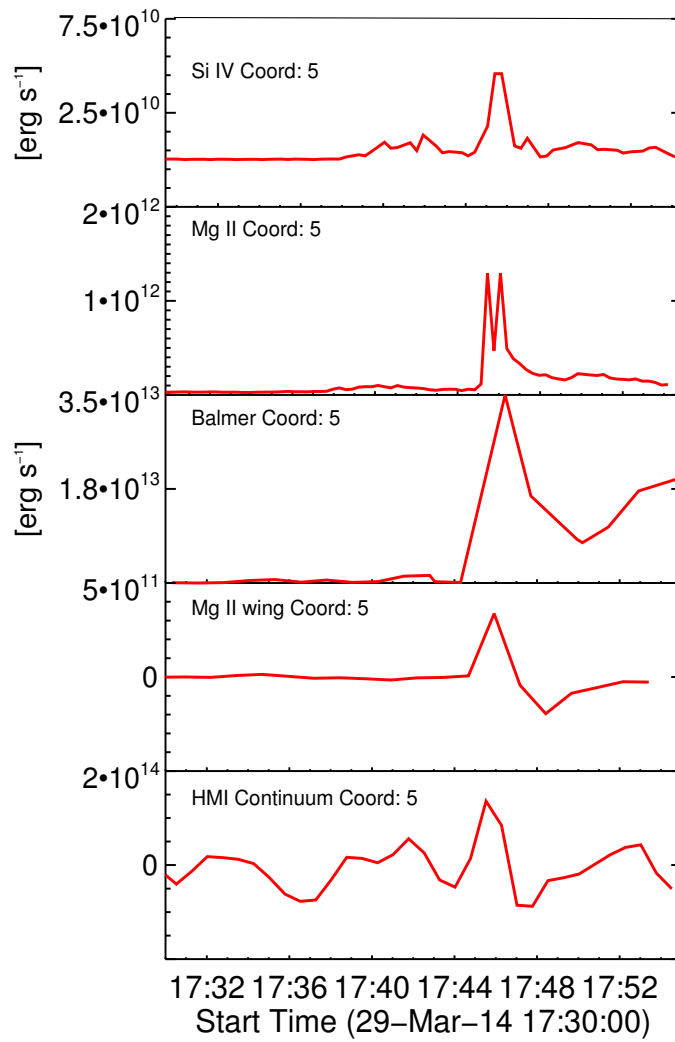


Figure 14: Shows radiative power from an area comparable to the sunquake impact, centered on region 5, which relates to heliocentric coordinates 524.3", 265.0". Each plot represents an independant data set, in order from top to bottom the sets are; IRIS SJ 1400 Å (Si IV); IRIS SJ 2796 Å (Mg II); IRIS SG 2825.7 to 2825.8 Å (Balmer Continuum); IRIS SJ 2832 Å (Mg II wing); SDO HMI continuum (HMI).

## Quake Location Energy Over Time

Power Radiated Over Sunquake Area (Central Coords 526.25",263.82")

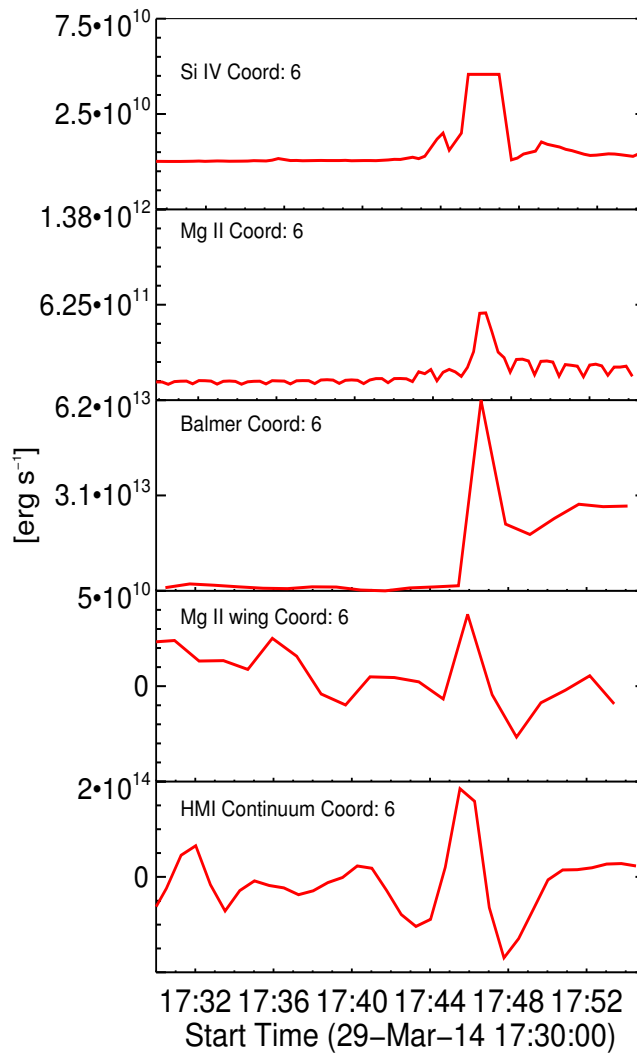


Figure 15: Shows radiative power from an area comparable to the sunquake impact, centered on region 6, which relates to heliocentric coordinates 526.3", 263.8". Each plot represents an independant data set, in order from top to bottom the sets are; IRIS SJ 1400 Å (Si IV); IRIS SJ 2796 Å (Mg II); IRIS SG 2825.7 to 2825.8 Å (Balmer Continuum); IRIS SJ 2832 Å (Mg II wing); SDO HMI continuum (HMI).



## References

- M. J. Aschwanden. *Physics of the Solar Corona. An Introduction with Problems and Solutions (2nd edition)*. December 2005.
- H. W. Babcock and H. D. Babcock. The Sun's Magnetic Field, 1952-1954. *ApJ*, 121:349, March 1955. doi: 10.1086/145994.
- P. Boerner, C. Edwards, J. Lemen, A. Rausch, C. Schrijver, R. Shine, L. Shing, R. Stern, T. Tarbell, A. Title, C. J. Wolfson, R. Soufli, E. Spiller, E. Gullikson, D. McKenzie, D. Windt, L. Golub, W. Podgorski, P. Testa, and M. Weber. Initial Calibration of the Atmospheric Imaging Assembly (AIA) on the Solar Dynamics Observatory (SDO). *Sol. Phys.*, 275:41–66, January 2012. doi: 10.1007/s11207-011-9804-8.
- D. C. Braun, C. Lindsey, Y. Fan, and S. M. Jefferies. Local acoustic diagnostics of the solar interior. *ApJ*, 392: 739–745, June 1992. doi: 10.1086/171477.
- J. C. Brown. The Deduction of Energy Spectra of Non-Thermal Electrons in Flares from the Observed Dynamic Spectra of Hard X-Ray Bursts. *Sol. Phys.*, 18:489–502, July 1971. doi: 10.1007/BF00149070.
- R. C. Canfield, T. R. Metcalf, D. M. Zarro, and J. R. Lemen. Momentum balance in four solar flares. *ApJ*, 348:333–340, January 1990. doi: 10.1086/168240.
- H. Carmichael. A Process for Flares. *NASA Special Publication*, 50:451, 1964.
- R. C. Carrington. Description of a Singular Appearance seen in the Sun on September 1, 1859. *MNRAS*, 20: 13–15, November 1859. doi: 10.1093/mnras/20.1.13.
- S. Couvidat, J. Schou, R. A. Shine, R. I. Bush, J. W. Miles, P. H. Scherrer, and R. L. Rairden. Wavelength Dependence of the Helioseismic and Magnetic Imager (HMI) Instrument onboard the Solar Dynamics Observatory (SDO). *Sol. Phys.*, 275:285–325, January 2012. doi: 10.1007/s11207-011-9723-8.
- B. De Pontieu, A. M. Title, J. R. Lemen, G. D. Kushner, D. J. Akin, B. Allard, T. Berger, P. Boerner, M. Cheung, C. Chou, J. F. Drake, D. W. Duncan, S. Freeland, G. F. Heyman, C. Hoffman, N. E. Hurlburt, R. W. Lindgren, D. Mathur, R. Rehse, D. Sabolish, R. Seguin, C. J. Schrijver, T. D. Tarbell, J.-P. Wülser, C. J. Wolfson, C. Yanari, J. Mudge, N. Nguyen-Phuc, R. Timmons, R. van Bezooijen, I. Weingrod, R. Brookner, G. Butcher, B. Dougherty, J. Eder, V. Knagenhjelm, S. Larsen, D. Mansir, L. Phan, P. Boyle, P. N. Cheimets, E. E. DeLuca, L. Golub, R. Gates, E. Hertz, S. McKillop, S. Park, T. Perry, W. A. Podgorski, K. Reeves, S. Saar, P. Testa, H. Tian, M. Weber, C. Dunn, S. Eccles, S. A. Jaeggli, C. C. Kankelborg, K. Mashburn, N. Pust, L. Springer, R. Carvalho, L. Kleint, J. Marmie, E. Mazmanian, T. M. D. Pereira, S. Sawyer, J. Strong, S. P. Worden, M. Carlsson, V. H. Hansteen, J. Leenaarts, M. Wiesmann, J. Aloise, K.-C. Chu, R. I. Bush, P. H. Scherrer, P. Brekke, J. Martinez-Sykora, B. W. Lites, S. W. McIntosh, H. Uitenbroek, T. J. Okamoto, M. A. Gummin, G. Auken, P. Jerram, P. Pool, and N. Waltham. The Interface Region Imaging Spectrograph (IRIS). *Sol. Phys.*, 289:2733–2779, July 2014. doi: 10.1007/s11207-014-0485-y.
- A.-C. Donea and C. Lindsey. Seismic Emission from the Solar Flares of 2003 October 28 and 29. *ApJ*, 630: 1168–1183, September 2005. doi: 10.1086/432155.
- A.-C. Donea, D. C. Braun, and C. Lindsey. Seismic Images of a Solar Flare. *ApJ*, 513:L143–L146, March 1999. doi: 10.1086/311915.
- T. L. Duvall, Jr., S. M. Jefferies, J. W. Harvey, and M. A. Pomerantz. Time-distance helioseismology. *Nature*, 362:430–432, April 1993. doi: 10.1038/362430a0.
- B. N. Dwivedi and F. b. E. N. Parker. *Dynamic Sun*. Cambridge University Press, Cambridge, UK, May 2003.
- P. V. Foukal. *Solar Astrophysics, 2nd, Revised Edition*. Wiley-VCH, 2004.
- T. Hirayama. Theoretical Model of Flares and Prominences. I: Evaporating Flare Model. *Sol. Phys.*, 34:323–338, February 1974. doi: 10.1007/BF00153671.
- H. S. Hudson. Thick-Target Processes and White-Light Flares. *Sol. Phys.*, 24:414–428, June 1972. doi: 10.1007/BF00153384.

- H. S. Hudson. Implosions in Coronal Transients. *ApJ*, 531:L75–L77, March 2000. doi: 10.1086/312516.
- H. S. Hudson, G. H. Fisher, and B. T. Welsch. Flare Energy and Magnetic Field Variations. In R. Howe, R. W. Komm, K. S. Balasubramaniam, and G. J. D. Petrie, editors, *Subsurface and Atmospheric Influences on Solar Activity*, volume 383 of *Astronomical Society of the Pacific Conference Series*, page 221, 2008.
- P. G. Judge, L. Kleint, A. Donea, A. Sainz Dalda, and L. Fletcher. On the Origin of a Sunquake during the 2014 March 29 X1 Flare. *ApJ*, 796:85, December 2014. doi: 10.1088/0004-637X/796/2/85.
- G. S. Kerr and L. Fletcher. Physical Properties of White-light Sources in the 2011 February 15 Solar Flare. *ApJ*, 783:98, March 2014. doi: 10.1088/0004-637X/783/2/98.
- R. A. Kopp and G. W. Pneuman. Magnetic reconnection in the corona and the loop prominence phenomenon. *Sol. Phys.*, 50:85–98, October 1976. doi: 10.1007/BF00206193.
- A. A. Korchak. Possible Mechanisms for Generating Hard X Rays in Solar Flares. *Soviet Ast.*, 11:258, October 1967.
- A. G. Kosovichev. Sunquake sources and wave propagation. In *Proceedings of SOHO 18/GONG 2006/HELAS I, Beyond the spherical Sun*, volume 624 of *ESA Special Publication*, page 134.1, October 2006.
- A. G. Kosovichev. Solar Oscillations. In J. A. Guzik and P. A. Bradley, editors, *American Institute of Physics Conference Series*, volume 1170 of *American Institute of Physics Conference Series*, pages 547–559, September 2009. doi: 10.1063/1.3246561.
- A. G. Kosovichev. Sunquakes: helioseismic response to solar flares. *ArXiv e-prints*, February 2014.
- A. G. Kosovichev and V. V. Zharkova. Seismic Response to Solar Flares: Theoretical Predictions. In *Helioseismology*, volume 376 of *ESA Special Publication*, page 341, 1995.
- A. G. Kosovichev and V. V. Zharkova. X-ray flare sparks quake inside Sun. *Nature*, 393:317–318, May 1998. doi: 10.1038/30629.
- A. G. Kosovichev and V. V. Zharkova. Magnetic Energy Release and Transients in the Solar Flare of 2000 July 14. *ApJ*, 550:L105–L108, March 2001. doi: 10.1086/319484.
- A. F. Kowalski, S. L. Hawley, M. Carlsson, J. C. Allred, H. Uitenbroek, R. A. Osten, and G. Holman. New Insights into White-Light Flare Emission from Radiative-Hydrodynamic Modeling of a Chromospheric Condensation. *Sol. Phys.*, June 2015. doi: 10.1007/s11207-015-0708-x.
- C. Lindsey and D. C. Braun. Helioseismic imaging of sunspots at their antipodes. *Sol. Phys.*, 126:101–115, March 1990. doi: 10.1007/BF00158301.
- C. Lindsey and D. C. Braun. Helioseismic Holography. *ApJ*, 485:895–903, August 1997.
- M. A. Livshits, O. G. Badalian, A. G. Kosovichev, and M. M. Katsova. The optical continuum of solar and stellar flares. *Sol. Phys.*, 73:269–288, October 1981. doi: 10.1007/BF00151682.
- M. E. Machado, A. G. Emslie, and J. C. Brown. The structure of the temperature minimum region in solar flares and its significance for flare heating mechanisms. *Sol. Phys.*, 58:363–387, July 1978. doi: 10.1007/BF00157282.
- M. E. Machado, A. G. Emslie, and E. H. Avrett. Radiative backwarming in white-light flares. *Sol. Phys.*, 124:303–317, September 1989. doi: 10.1007/BF00156272.
- J. C. Martínez-Oliveros and A.-C. Donea. Magnetic field variations and seismicity of solar active regions. *MNRAS*, 395:L39–L42, May 2009. doi: 10.1111/j.1745-3933.2009.00637.x.
- J. C. Martínez-Oliveros, H. Moradi, and A.-C. Donea. Seismic Emissions from a Highly Impulsive M6.7 Solar Flare. *Sol. Phys.*, 251:613–626, September 2008. doi: 10.1007/s11207-008-9122-y.
- S. A. Matthews, L. van Driel-Gesztelyi, H. S. Hudson, and N. V. Nitta. A catalogue of white-light flares observed by Yohkoh. *A&A*, 409:1107–1125, October 2003. doi: 10.1051/0004-6361:20031187.

- D. F. Neidig and E. W. Cliver. The occurrence frequency of white-light flares. *Sol. Phys.*, 88:275–280, October 1983. doi: 10.1007/BF00196192.
- E. Pedram and S. A. Matthews. A Survey of the Hard X-Ray Characteristics of Seismically Active and Quiet White-Light Flares. *Sol. Phys.*, 277:317–335, April 2012. doi: 10.1007/s11207-011-9922-3.
- E. R. Priest. *Solar magneto-hydrodynamics*. D.Reidel Publishing Company, Dordrecht, Holland, 1982.
- F. Roddier. Principle of production of an acoustic hologram of the solar surface. *Academie des Sciences Paris Comptes Rendus Serie B Sciences Physiques*, 281:93–95, July 1975.
- K. Shibata and T. Magara. Solar Flares: Magnetohydrodynamic Processes. *Living Reviews in Solar Physics*, 8:6, December 2011. doi: 10.12942/lrsp-2011-6.
- P. A. Sturrock. Model of the High-Energy Phase of Solar Flares. *Nature*, 211:695–697, August 1966. doi: 10.1038/211695a0.
- Z. Svestka. Solar flares. *Geophysics and Astrophysics Monographs*, 8, 1976.
- C. L. Wolff. Free Oscillations of the Sun and Their Possible Stimulation by Solar Flares. *ApJ*, 176:833, September 1972. doi: 10.1086/151680.
- S. Zharkov, L. M. Green, S. A. Matthews, and V. V. Zharkova. 2011 February 15: Snuquakes Produced by Flux Rope Eruption. *ApJ*, 741:L35, November 2011. doi: 10.1088/2041-8205/741/2/L35.
- S. Zharkov, L. M. Green, S. A. Matthews, and V. V. Zharkova. Properties of the 15 February 2011 Flare Seismic Sources. *Sol. Phys.*, 284:315–327, June 2013. doi: 10.1007/s11207-012-0169-4.
- V. V. Zharkova and S. I. Zharkov. On the Origin of Three Seismic Sources in the Proton-rich Flare of 2003 October 28. *ApJ*, 664:573–585, July 2007. doi: 10.1086/518731.